



Institute of Biomechanics
Center of Biomedical Engineering
Stremayrgasse 16/2
8010 Graz, Austria

Master Thesis

Ultrastructural investigation of biaxially loaded
human aortic tissue

to achieve the degree of
Master of Science

Author: Anna-Sophie Wittgenstein

Supervisor: Gerhard Sommer, PhD

Head of Institute: Professor Gerhard A. Holzapfel, PhD

Graz, October 23, 2018

STATUTORY DECLARATION

I declare that I have authored this thesis independently, that I have not used other than the declared sources / resources, and that I have explicitly marked all material which has been quoted either literally or by content from the used sources.

.....
date

.....
(signature)

EIDESSTATTLICHE ERKLÄRUNG

Ich erkläre an Eides statt, dass ich die vorliegende Arbeit selbstständig verfasst, andere als die angegebenen Quellen/Hilfsmittel nicht benutzt, und die den benutzten Quellen wörtlich und inhaltlich entnommenen Stellen als solche kenntlich gemacht habe.

Graz, am

.....
(Unterschrift)

Abstract

The leading cause of deaths world wide are diseases of the cardiovascular system especially involving diseases of the the aorta. The alterations of aortic wall with age, diet and life style are severe and require further research for a deeper understanding of the underlying mechanics.

This thesis is part of a FWF funded project which aims to relate mechanical stress to structural changes of aortic tissue on a multiscale level. The objective of this thesis was to establish a workflow to determine structural and mechanical properties of human aortic tissue on the nano-scale in order to develop material models for further FE analysis in cooperation with the Gottfried Schatz Centre, Medical University Graz. The human aortic tissue samples used were obtained from the Department of Pathology. All three layers intima, media, adventitia of arterial walls were characterised individually in-plane after mechanical testing. Each layer has different structure, constituents and function. Therefore the focus of this study was the connection between collagen and proteoglycans in all three layers. After tracking the deformation at different macroscopic biaxial loads with a CCD camera, transmission emission microscopy is used to visualise the changes in the ultrastructure of collagen and proteoglycans in the tissue. The open source software "SerialEM" is used to generate tilt series which enables the 3D reconstruction of the stretch-dependent properties, especially the mean fibre direction and dispersion with IMOD and AMIRA[®] Software.

The chosen protocol provided well fixed biaxially stretched tissue and the identification of collagen fibrils and proteoglycans under transmission electron microscopy was sufficient to visualise a 3D volume. The mechanical response of all healthy tissue samples showed an anisotropic and linear elastic behaviour at low stresses followed by stiffer nonlinear response at high stretches. The atherosclerotic tissue could not be stretched to the desired amount without rupture at attachment points and displayed a overall stiffer mechanical response.

Kurzfassung

Erkrankungen des Herz-Kreislauf-Systems, insbesondere Erkrankungen der Aorta, sind weltweit die häufigste Todesursache. Die Veränderungen der Aortenwand mit Alter, Diät und Lebensstil sind schwerwiegend und erfordern Grundlagenforschung für ein besseres Verständnis der zugrunde liegenden Mechanik.

Diese Diplomarbeit ist Teil eines vom FWF geförderten Projekts, das sich auf die Wechselwirkung mechanischer Belastung und strukturellen Veränderungen von Aortengewebe auf einer Multiskalenebene bezieht. Die Etablierung eines Arbeitsablaufs in Kooperation mit der Medizinischen Universität Graz zur Bestimmung struktureller und mechanischer Eigenschaften des menschlichen Aortengewebes im ultrastrukturellen Bereich war Ziel dieser Arbeit. Die menschlichen Aortengewebeproben wurden vom Institut für Pathologie bezogen. Alle drei Schichten - Intima, Media, Adventitia - der Arterienwände wurden nach der mechanischen Prüfung einzeln in axialer Richtung untersucht. Jede Schicht weist unterschiedliche Struktur, Bestandteile und Funktion auf, daher liegt der Fokus dieser Studie auf der Verbindung zwischen Kollagenfasern und Proteoglykanen in allen drei Schichten. Nach dem Aufzeichnen der Deformation bei verschiedenen makroskopischen biaxialen Belastungen mit einer CCD-Kamera, wurde Transmissionselektronenmikroskopie verwendet, um die Veränderungen in der Ultrastruktur von Kollagen und Proteoglykanen im Gewebe zu visualisieren. Die Open-Source-Software "SerialEM" wurde zur Generierung von Tilt-Serien verwendet, die die 3D-Rekonstruktion der dehnungsabhängigen Eigenschaften ermöglicht, insbesondere die durchschnittliche Faserorientierung und Dispersion mittels IMOD und AMIRA Software.

Das durchgeführte Protokoll fixierte das biaxial gestreckte Gewebe ausreichend und ermöglichte die Identifizierung von Kollagenfibrillen und Proteoglykanen mit dem Transmissionselektronenmikroskop für die Generierung von 3D-Volumen. Die mechanische Antwort aller gesunden Gewebeproben zeigte anisotropes und linear elastisches Verhalten im niedrigem Dehnungsbereich und steiferes nicht lineares Verhalten in hohem Dehnungsbereich. Das atherosklerotische Gewebe konnte nicht auf die geplante Größe gestreckt werden, ohne bei den Befestigungshaken zu reißen und zeigten dabei eine allgemein steiferes mechanisches Verhalten.

Acknowledgement

The cooperation between the Institute of Biomechanics, Graz University of Technology and the Medical University Graz was the foundation of this thesis. I would like to express my gratitude to all people who supported the project and me during this process.

First I would like to thank my supervisor Dr. Gerhard Sommer for establishing the project and the trust he showed towards me during the last year. In the course of this thesis I not only gained a lot of knowledge but also about working with a team of researchers which would not have been possible without him and his knowledge. My gratitude towards the head of the Institute of Biomechanics, Graz, Prof. Dr. Gerhard Holzapfel, for welcoming me to the Institute and for providing the laboratory facilities for this master thesis is only exceeded by his incredible influence in me getting a PHD position at KCL.

A special thanks goes out to the Electron Microscopy Team at the Medical University Graz without them it would not have been possible to handle the workload of this project. Not solely your contribution of knowledge but especially your friendship has carried me through this work and made me feel special.

My time studying in Graz was always accompanied by great friendships and I want to use this opportunity to thank all of them. Without you I could not have done it. Last but not least I would like to thank my family.

Meiner Schwester Laura möchte ich für all unsere schönen Abenteuer in den letzten Jahren danken. Unsere Freundschaft und die positive Energie in den schweren Zeiten sind mir eine enorme Stütze die ich täglich schätze. Danke Renate, für die Unterstützung dieser Verbindung.

Meinen Eltern möchte ich nicht nur für die Ermöglichung meines Studiums danken, sondern vor allem für ihre Liebe und ihr Vertrauen. Vielen Dank, dass ihr mir von klein auf die Welt gezeigt habt und mich zu dem Menschen erzogen habt, der ich heute bin. Danke für den sicheren Hafen, der mir unglaublich viel Stabilität gibt und mir ermöglicht mich fallen zu lassen.

Contents

Statutory	i
Abstract	iii
Kurzfassung	v
Acknowledgement	vii
1. Introduction	1
1.1. Motivation	1
1.2. Histology of Arterial Wall	2
1.2.1. Layers	2
1.2.2. Components	4
1.3. Atherosclerosis	7
1.4. Transmission Electron Microscope	8
1.4.1. Principal Image Acquisition	8
1.4.2. Tomography	9
2. Materials & Methods	11
2.1. Sample Preparation	11
2.2. Preconditioning & Fixation of Specimen	13
2.3. Embedding	14
2.4. Sectioning	19
2.4.1. Microtome	19
2.4.2. Stainer	19
2.4.3. Fiducial Markers	21
2.5. Transmission Electron Microscope	21
2.6. Test Data	25
3. Results	27
3.1. Biaxial Test	27
3.2. Ultrastructural Investigation	31
3.2.1. Light Microscope Images	31
3.2.2. TEM Image Acquisition	36
3.2.3. Tilt Series Acquisition	39

3.2.4. Tomogram	40
3.2.5. 3D-Amira [®] Reconstruction	41
4. Discussion	45
A. Testing Data Plots	49
Abbreviations	63
References	65

1. Introduction

1.1. Motivation

This Master Thesis is part of a research project, *Multiscale biomechanical investigation of human aortas* performed at the Institute of Biomechanics, Graz University of Technology in cooperation with the Gottfried Schatz Centre, Medical University Graz, and is funded by the FWF. This project aims to relate changes in the tissue on different scale levels to mechanical stress. Therefore the main focus of thesis was to establish a work flow to investigate aortic tissue in a transmission electron microscope.

A healthy heart beats about 100000 times a day, therefore it is important to understand the effects of hemodynamics (especially altered) on the human aorta [8]. This multi-scale approach tries to set underlying mechanisms of atherosclerosis and tissue failure into context.

Macroscopic mechanical behaviour changes due to structural alterations on the micro and nano scale and therefore it is of utmost importance to relate these changes to one another. Especially the mechanical and structural differences between healthy and atherosclerotic tissue will generate data for computational modelling to further investigate the progression of atherosclerosis. An experimental setup at the Institut of Biomechanics to biaxially stretch the human tissue to determine the mechanical response and to observe the ultrastructural changes of the tissue at the Gottfried Schatz Centre can help understand, e.g amongst others the effects of dilatation processes of aortic tissue in cardiac distress [12].

The combination of sectioning biaxially tested human abdominal aorta for transmission electron microscopy and reconstructing a 3D volume of collagen fibrils with proteoglycans has not been mentioned in the literature and enables measuring important structural and geometrical parameters for modelling. This investigations seek to asses the differences of the loaded and unloaded conditions of the tissue for a better understanding of the underlying mechanisms of structural changes in health and disease [15].

This project is a fundamental research and is an ongoing process, where protocols have been established and optimised for the used workflows. Based on the results new multiscale projects will be designed and performed at the Institute of Biomechanics in the near future.

1.2. Histology of Arterial Wall

According to their characteristics and function human arteries are roughly classified into elastic and muscular arteries. Elastic arteries are the largest vessels in the human body and are located relatively close to the heart, this includes the ascending, thoracic and abdominal aorta. The group of elastic arteries smooth the pulsatile blood output of the heart into a continuous flow [8]. With increasing distance to the heart the elastic content in arterial walls decreases and is replaced by smooth muscle cells (SMCs) to regulate the blood flow by vasoconstriction or vasodilatation [23]. Due to the transformation from the elastic to the muscular type, arteries with both morphological features can be found.

1.2.1. Layers

The microscopic structure of blood vessels is composed of three layers, the intima (*tunica intima*), the media (*tunica media*) and adventitia (*tunica adventitia*) as shown in Fig 1.

Intima The inner coating of elastic arteries are formed by a single sheet of flattened and elongated endothelial cells connected to a thin basal lamina. Underneath the subendothelial layer varies in thickness with topography, age and disease due to the collagen and elastic fibres content. In healthy arteries the intima is a gateway for chemical signals and supplies the vessel wall with nutrients from the bloodstream. In contrast to functional importance the contribution of intima to the mechanical response of arterial walls is negligible in health. Due to thickening of the intimal layer the contribution to the mechanical response is higher with age and sickness [7].

Media The internal elastic lamina (IEL) separates the intima from media and is considered to be part of the latter. This lamina is a perforated sheet of elastin permitting the transfer of nutrients and electrolytes through the arterial wall. The media in elastic arteries consist of elastic lamellar units containing SMCs and fenestrated sheets of elastic fibres interwoven with collagen fibrils (collagen fibre bundles 30% type I and 70% type III [16,25]) surrounded by ground substance containing proteoglycans (PGs) [8]. In elastic arteries the basic functional and structural unit

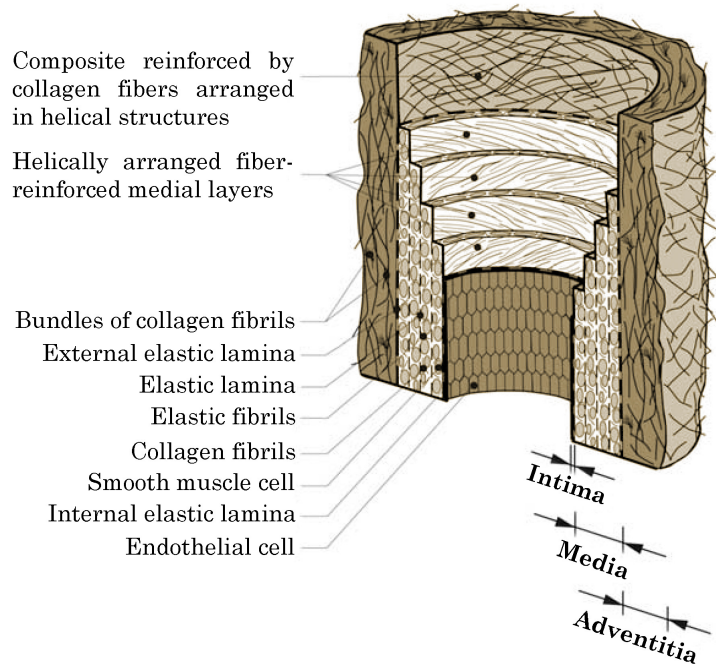


Figure 1: Diagrammatic model of the layers of arterial wall and their constituents [7]

is called "musculo-elastic fascicle" [1]. The number of these units depends on the diameter of the vessel eg. in the abdominal aorta there the media has 40 – 70 layers of these units [9]. In the mechanical context the media is under regular physiological *in vivo* conditions the most significant layer [8]. The external elastic lamina (EEL) is the outermost sheet of the media and is the border to the adventitia.

Adventitia The adventitia is the outermost layer of arteries and is composed of a network of collagen fibres intermixed with fibroblasts, elastin, nerves and vasa vasorum providing thicker arterial walls with blood. The intramural network is highly dependent on the topology and diameter of the vessel [9, 28]. The fibroblasts are predominantly responsible for synthesising collagen fibres (mainly type I) [9]. The undulated and in helices arranged collagen fibrils act as a protective sheet for the vessel and limit severe overdistension [7]. Hence, the gradually stiffening of the collagen fibres at higher levels of pressure. Perivascular adipose tissue is juxtaposed to the adventitia and embeds the vessel and provides structural support although the exact mechanical significance has not been determined yet [4].

1.2.2. Components

Endothelial cells, smooth muscle cells and extracellular matrix (ECM) are the main histological components of arteries. The focus of this thesis are collagen fibres and proteoglycans. Therefore, these are the two constituents of the ECM being described for a better overview in this section.

Collagen Collagen can be found in almost all connective tissues and is a main load carrying element. It is the most frequently occurring structural protein in the human body and 28 different types have been detected up to now. In line with this thesis about the cardiovascular system Types I,III–VI and VIII are the most abundant forms, which are synthesised by SMCs and fibroblasts. The half-life of these collagen types in arterial walls seem to be in the order of 15–90 days and to maintain the physiological integrity of arterial walls synthesis and degradation of collagen needs to be balanced [6].

Three amino polypeptide strands (α -chains) form a *tropocollagen* (collagen molecule) with about 285 nm length, each strand is a left-handed helices. They organise into a right-handed triple-helix stabilised by hydrogen bonds (intramolecular cross-links) between the α -chains [5] as depicted in Fig 2. Five of these structures assemble to collagen fibrils stabilised by covalent cross-links with 100–200 μm in length and 10–500 nm in diameter. Collagen fibrils further organise themselves ultimately to undulated collagen fibres. The repeating quater-staggered groups enable the clear identification of collagen in transmission electron microscopes [9].

Proteoglycan Proteoglycans are a genetically unrelated group of multi-domain proteins with covalently attached glycosaminoglycan chains (GAG), see Fig. 3(a), which are long branchless biopolymers with repeating disaccheride units [6,11]. Therefore PGs have an important role in vascular structure and are believed to be involved in intrafibrillar connectivity and matrix-cell communication [5].

Versican belongs to the group of large proteoglycans and is a constituent of the ECM in aortic tissue [29]. Besides growth factors, enzymes and other ECM components it binds hyaluronan (GAG) to fill the ECM with viscoelastic high molecular weight complexes. Therefore it is an important constituent regarding fluid dynamics in the

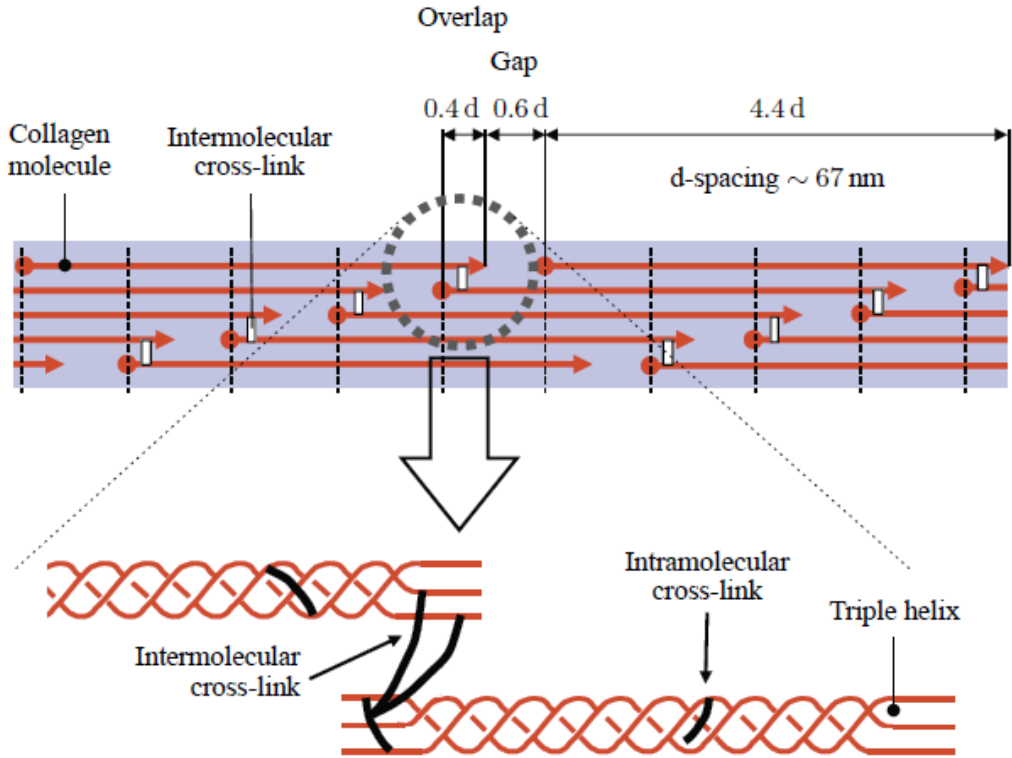


Figure 2: Hierarchical organisation of tropocollagen to collagen fibrils with periodic d-spacing of 67 nm and schematic illustration of cross-links between each of the ~1.4 nm molecules (intra) and in between them (inter). Image taken from [6].

vessel wall [26]. Decorin, biglycan and lumican are parts of small leucine rich proteoglycans (SLRPs) and can bind ECM molecules like collagen, fibronectin and fibrillin-containing microfibrils. The crescent shape of the decorin core protein complex as depicted in Fig. 3(b) enables the enclosing of a single collagen fibril by recognising a specific sequence [5,11,24]. In contrast to localising biglycan in all layers decorin was detected only in the adventitia [22].

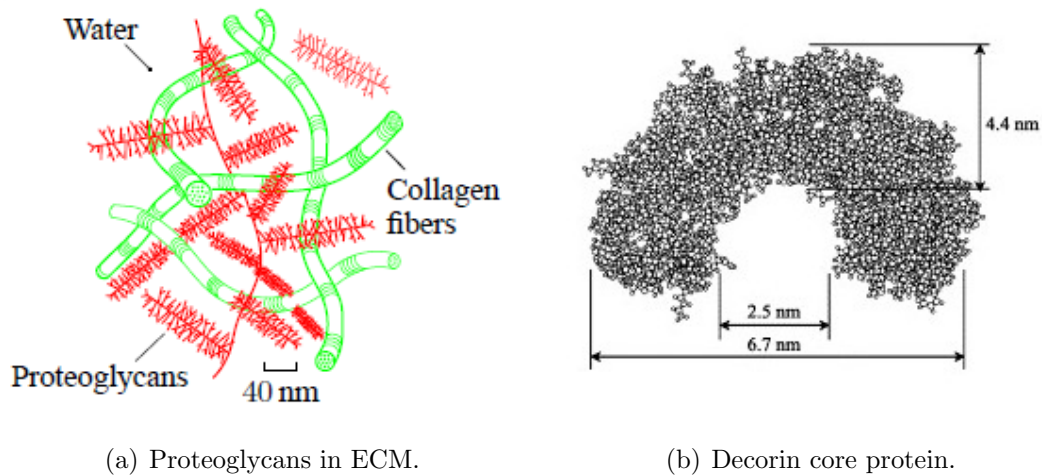


Figure 3: (a) Schematic **proteoglycans** forming high molecular weight complexes in the extra cellular matrix with **collagen fibres**, taken from [6]. (b) Molecular model of a decorin core protein molecule with a u-shaped form for binding a collagen molecule [24]. Reprinted with permission from Elsevier.

1.3. Atherosclerosis

Atherosclerosis is a progressive disease altering the arterial wall composition and mechanics and it is the leading cause of death world wide¹. Although there are still different theories on the etiology of atherosclerosis some risk factors like age, gender, smoking, adiposity and others have been determined. Atherosclerosis occurs in arteries with different blood flow dynamics (e.g. carotid bifurcation) resulting in wall changes, loss of elasticity and reduction of the lumen [15].

The progression of atherosclerosis, as schematically illustrated in Fig (4) is indicated by entry of an increasing amount of cholesterol-containing low-density lipoproteins (LDL) into the intima due to changes in extracellular matrix composition and lower permeability caused by inflamed endothelial cells of the intima which express adhesion molecules enabling leukocytes to bind on the surface [21]. After migrating into the intima monocytes differentiate to tissue macrophages and become foam cells by ingesting lipoprotein particles [14]. Further atheroma formation induces migration of SMCs from media to intima which proliferate and release extracellular matrix molecules like interstitial collagen and elastin.

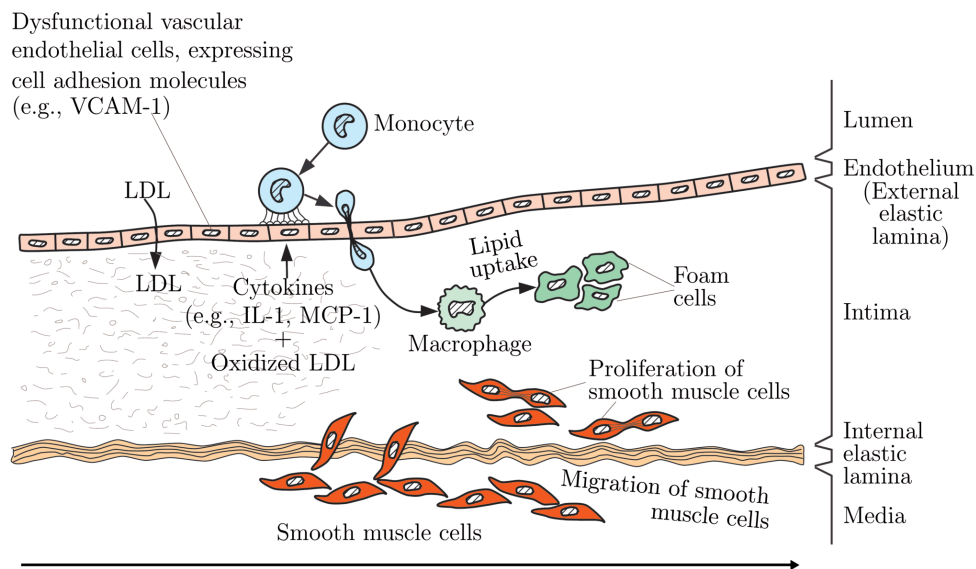


Figure 4: Schematic model of the development of atherosclerosis. Arrow indicates the disease progression [19]

¹<http://www.who.int/news-room/fact-sheets/detail/the-top-10-causes-of-death>

This network covers the plaque like a protective sheet and is known as fibrous cap. The entrapped dead foam cells release lipids and can promote the formation of a necrotic core of the plaque [20]. The increased size of the plaque causes malnutrition of the arterial wall and may lead to formation of micro vessels and cholesterol crystals. At this late stage a stable plaque is only affecting the circulation in contrast to an unstable plaque, which increases the risk of rupturing and inducing thrombus formation [14].

1.4. Transmission Electron Microscope

1.4.1. Principal Image Acquisition

Transmission electron microscopes (TEM) work in analogy to normal light microscopy, but instead of photons it uses electrons. A simplified illustration of using the wave-like character of electrons - an electron beam interacts with a thin section and the electrons are then used to generate a image of the investigated area [2].

The electron beam is emitted from the upper end of the TEM, see Fig. fig:tecnai, by applying a strong current between a cathode and an anode.



Figure 5: Electron Transmission Microscope FEI Tecnai™ F20 ©FEI Company.

A filament is heated to accelerate the electrons into the direction of the anode and are focused by electromagnets. Before the electron beam penetrates the samples an aperture decreases the intensity [13]. Specimen sections are placed into the TEM with the help of a sample holder which can be moved to view the whole grid. Interaction between the electron beam and atoms of the section causes energy loss, called inelastic scattering, hence different grey values in the image. To increase scattering contrast pre- and post-embedding staining with heavy metals of the specimen is used [2]. These effects can be observed either on a fluorescent screen or by a bottom mount camera which creates images through a charge-coupled device (CCD) camera.

1.4.2. Tomography

The acquisition of a two-dimensional projection of tissue as explained before is not suited to deliver information about the relative location within the samples. Serial sectioning TEM is a highly error-prone process. Therefore the tomography technique is a better way to get three-dimensional information about the ultra-structure of tissue.

In Fig. 6 the two principal steps of tomography are depicted, first it is necessary to obtain as many viewing directions as possible, this is dependent on sample holder, used grid and position of the section on the grid. In practice the tilting angles are between -60 and $+60$ where images are taken at tilt intervals of 1° , illustrated in Fig. 6(a). These so-called tilt-series are then reconstructed through a real-space weighted back-projection. A point is described by two "rays" therefore the more complex a structure is the more "rays" are needed to describe it. The weighted inversion of the tilt-series project "rays" that describe the structure in the projection direction and through superposition from different angles the shape of the structure is generated, as schematically shown in Fig. 6(b).

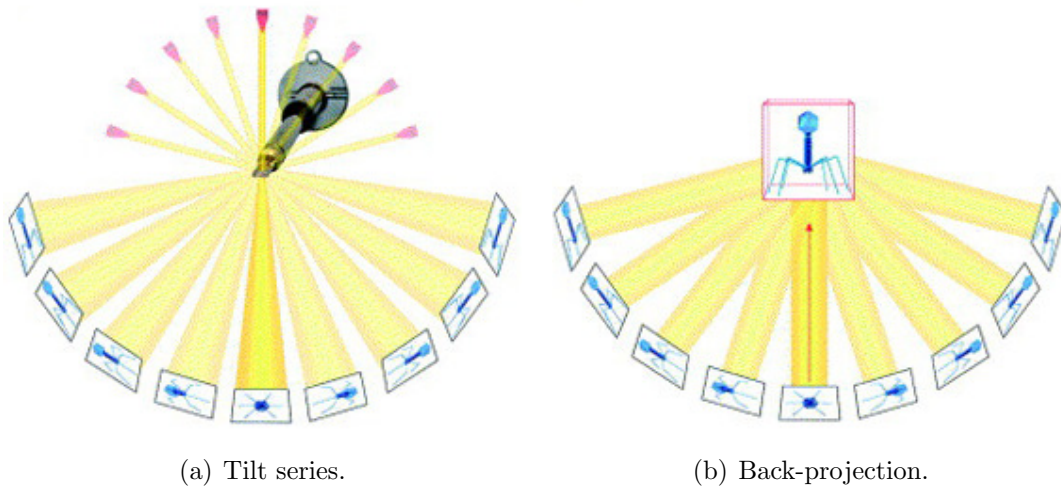


Figure 6: Principal of TEM Tomography. (a) A specimen, here a bacteriophage placed in a TEM sample holder is imaged by tilting the holder and acquiring a image at each tilt. (b) Schematic process of the computed back-projection, where each angle contributes to reconstructing the original structure [17]. Reprinted with permission from Elsevier.

2. Materials & Methods

This section provides an overview of the steps performed on the abdominal aortic tissue, from sample preparation for mechanical testing, embedding and cutting the tissue, recording the tilt-series in TEM, reconstruction of the tomogram with IMOD software to visualise the tomogram with *Amira*[®] software.

The abdominal aortic tissue is obtained from the Institute of Pathology, Medical University Graz, the mechanical testing is performed at the Institute of Biomechanics, Graz University of Technology and the embedding, cutting, imaging and visualisation is performed at the Research Unit Electron Microscopic Techniques, Medical University of Technology.

2.1. Sample Preparation

After transporting the tissue as fast as possible from the Institute of Pathology to the Institute of Biomechanics the aortic tissue, as shown in Fig.7 is cut open to get a planar specimen enabling the stamping of 20×20 mm square-shaped specimens.



Figure 7: Abdominal aortic tissue from Institute of Pathology with surrounding connective tissue which needs to be removed before testing without harming the adventitia. The photographed centimeter scale provides a dimensional reference.

In order to biaxially stretch the tissue it is necessary to establish a connection between the tissue and the testing device. Therefore the tissue is hooked up with five fish hooks attached to a suture thread on each edge of the squared tissue.

This setup is based on a paper by Eilaghi et al. [3] about the impact of attachment points to the uniform distribution of strain in the tissue which is shown in Fig. 8. Hence the assumption that it is the same for stress field distribution throughout the tissue sample. Furthermore it must be stated that their findings are based on a rubber template. Eilaghi et al. suggest to choose five attachment points per side located 0.6 to 1.0 times the spacing between attachment points away from the edge.

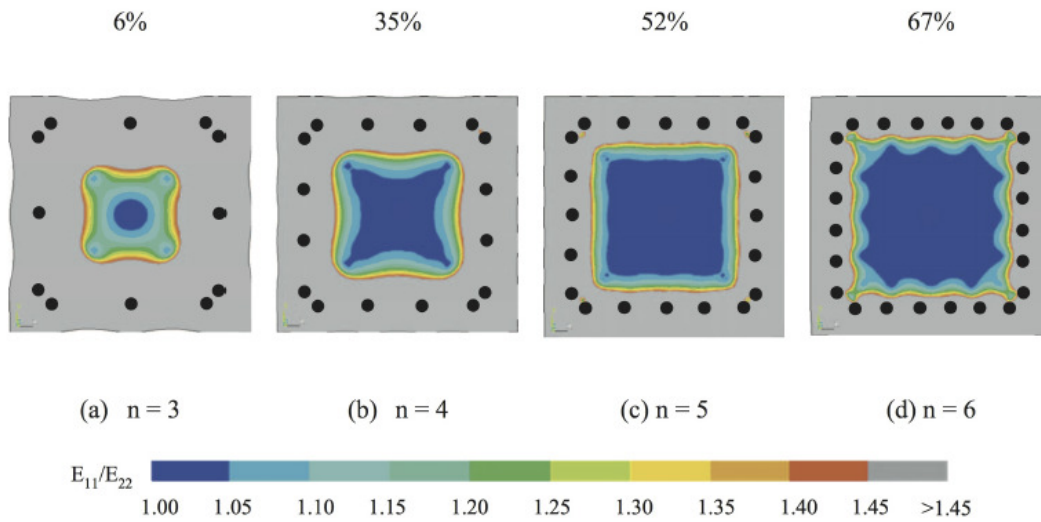


Figure 8: Effect of changing the number of attachment points n along each side to the strain field inside the tissue, as indicated by the color contour plots. The black dots indicate the attachment points and are drawn to scale. The percentages on top of each tissue sample indicate the fraction of the interior area where the principal strain ratio is sensibly constant. Reprinted from [3].

Our hooking pattern is shown in Fig. 9(a) and was printed onto a plastic foil which was punched through the attachment points to enable the exact marking of the tissue with surgical markers (slightly hinted in purple in Fig. 9(b)). It is very important to keep track of the orientation in respect to the axial direction of the tissue and to keep the tissue moist with phosphate-buffered saline solution (PBS). Meanwhile a cruciform basin full of PBS solution is heated to 37°C to establish a physiological

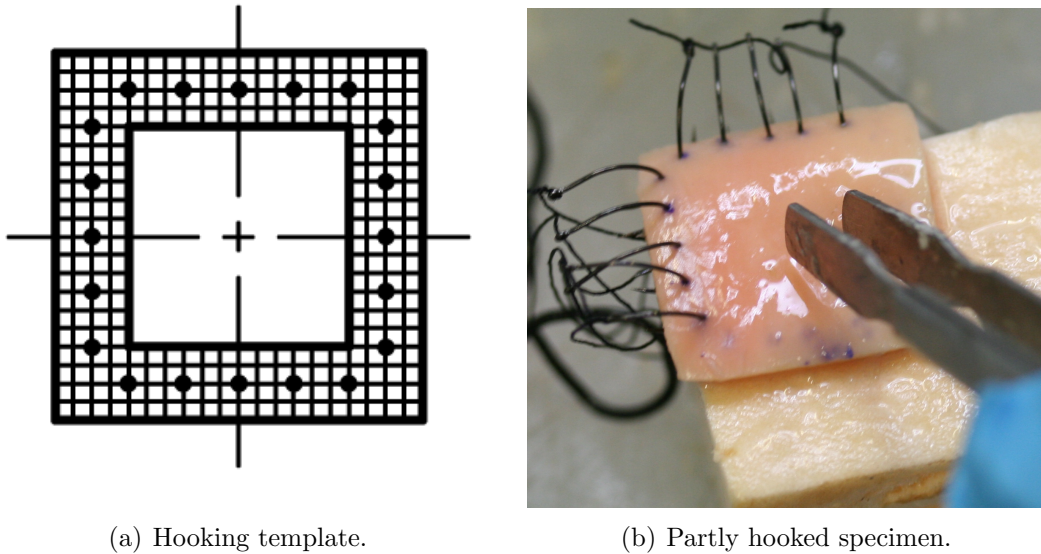


Figure 9: Hooking geometry of the specimen (a) The template with 20×20 mm boarder and 3 mm distance between the hooking points and 2 mm from the outside border. (b) Abdominal aortic tissue stamped as the template and hooked up at 10 out of 20 hooking points.

environment for the sample during preconditioning. Further it is necessary to work as fast as possible to keep the autolysis of the tissue to a minimum without harming the tissue with tweezers or neglecting precession.

Once the specimen is hooked up it gets mounted into the biaxial tensile testing device in a trampoline fashion and the tissue gets marked for better feature tracking. The testing device was developed in cooperation between the Institute of Biomechanics with the company Messphysik, Fürstenfeld for tests on biological and artificial tissue samples like our setup in Fig. 10.

2.2. Preconditioning & Fixation of Specimen

To optimise feature tracking by the optical detection system, a small petri dish was positioned over the specimen to get rid of reflections of the PBS solution and light interferences. It is necessary to calibrate the video-extensometer to determine the starting position of the four linear drives. Afterwards the mounted tissue was exposed to an approximate preloading between 0.015 and 0.020 N. The deformation

was achieved through the drifting outwards from the center in both directions of the linear drives. During this deformation process the tissue is exposed to stress relating to forces which were registered by the four load cells. The tests were carried out at a testing speed of 3 mm/min until specific stretch levels to mimic quasi-static deformation. The different stretch levels (5%, 10%, 15% and 20%) were applied starting at the lowest stretch and for each level five preconditioning and one testing cycle were performed before the device was stopped at the designated stretch level. During preconditioning the thickness of each specimen was measured optically, hence each cycle is composed of loading and an unloading. The testing protocol saved different parameters into an excel sheet. The parameters are the applied forces, the covered distances of the carriages and the recorded distance between the initial tracking points and the covered way during stretching and relaxing. After stopping the device at the specific stretch value, the PBS solution was changed to glutaraldehyde (GA) to fixate the stretched specimen for four hours, see Fig. 10.

2.3. Embedding

The under stretch fixated aortic tissue, see Fig. 11(a), is marked by cutting off the upper right part of the squared tissue and put into a flask filled with 0.1 M sodium-phosphate buffer with a pH 7.4 in order to not loose the orientation (axial and Intima-Media-Adventitia). Three small enough pieces ($\sim 4 \times 2$ mm) are cut out of the gage region of the specimen, as schematically depicted in Fig. 11(b), at the Medical University Graz. This is done to ensure chemicals from the following protocol in Tab.1 permeate the whole sample equally and the specimen fits into the later introduced embedding mould. The sample gets stained with 1% Cuproline Blue (CB) for contrasting the proteoglycans, see paragraph 1.2.2 for TEM [27]. The residual stain material gets washed out with acetate buffer with $MgCl_2$ and incubated in 0.5% sodium tungstic acid in acetate buffer and afterwards in ethanol over night in the fridge. The next day they are rinsed with distilled water and block stained with 1% uranyl acetate (UA) in acetate buffer to emphasize collagen fibrils. Before the specimen is hydrated with a graduated concentration of ethanol it gets washed in 0.1 M maleate buffer and in bi-distilled water, if necessary the tissue could be stored over the weekend at the 70% ethanol concentration step in the fridge. Using a intermedium of

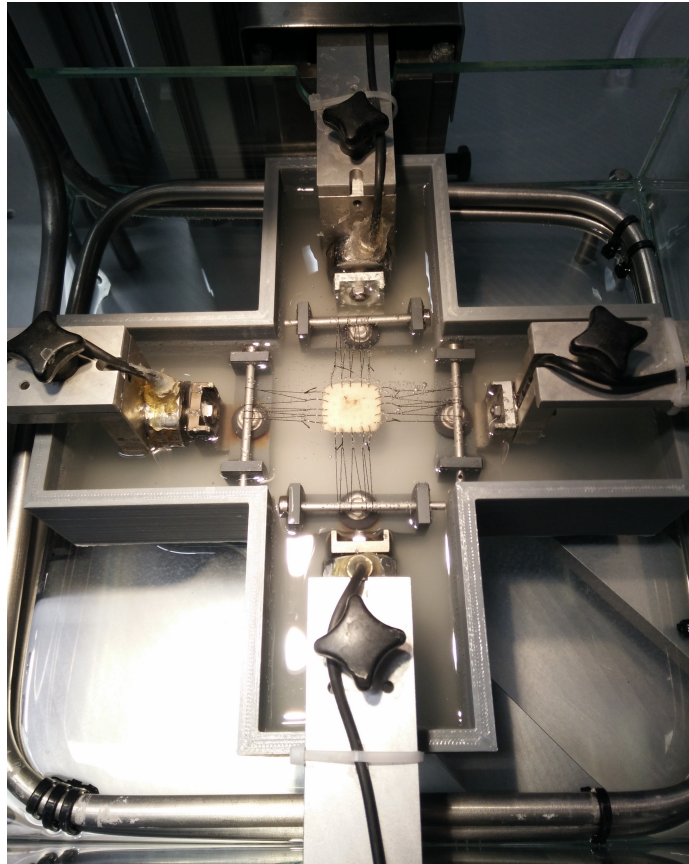
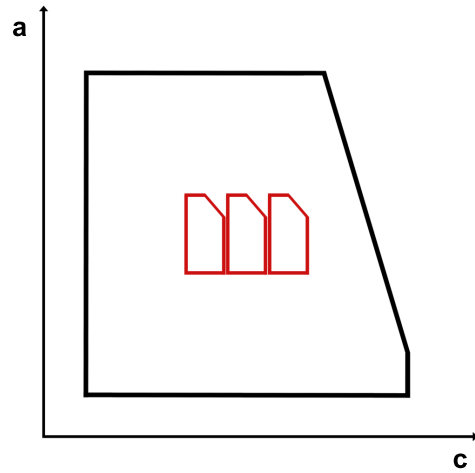


Figure 10: Biaxial testing device with hooked tissue sample under stretch in GA for fixation.



(a) Stretched and fixed tissue.



(b) Marking pattern.

Figure 11: Marking of the fixated tissue to keep orientation. (a) Sample after fixation in GA under stretch for four hours, in black you see the afore mentioned paint for feature tracking. (b) First and **second** marking pattern for further steps.

propylene oxide and epoxy resin (TAAB[®]) the tissue gets completely infiltrated with resin following a step-by-step approach see Tab.1. For sufficient polymerisation of the resin block with the aligned tissue, see Fig. 12(b), the embedding mould is incubated at 60 °C for three days. The embedded tissue as in Fig. 12(b) can be sectioned with an ultramicrotome, described in the following paragraph.

Table 1: Embedding protocol for visualising collagen fibrils and proteoglycans.

Step	Solution	Duration
Fixation	2% Glutaraldehyde diluted in PBS	4 h
Staining	1% CB in 0.2 M acetate buffer + 0.3 M $MgCl_2$	O/N
	wash with 0.2 M acetate buffer + 0.3 M $MgCl_2$	3x 10 min
	0.5% $NaWO_4$ in 0.2 M acetate buffer	1 h
	0.5% $NaWO_4$ in 30% EtOH at 4 °C	O/N
	wash with Aqua bidest.	3x 10 min
	1% UA in 0.1 M acetate buffer (covered)	1 h
	wash with 0.1 M maleate buffer	3x 10 min
	wash with Aqua bidest.	3x 10 min
Dehydration	50% EtOH	30 min
	70% EtOH	O/N
	80% EtOH	30 min
	96% EtOH	30 min
	100% EtOH	15 min
	100% EtOH	15 min
Intermedium	propylene oxide	1h
	propylene oxide/TAAB 1+1	3h
	propylene oxide/TAAB 1+2 at 4 °C	O/N
	TAAB at 45 °C	2x 90 min
Polymerisation	Put TAAB into embedding mould and put the aortic tissue with the axial direction of the tissue in parallel with the bottom line of the embedding form 12(a).	
	Align specimen - intima facing outward - and put embedding mould into incubator at 60 °C.	3 days

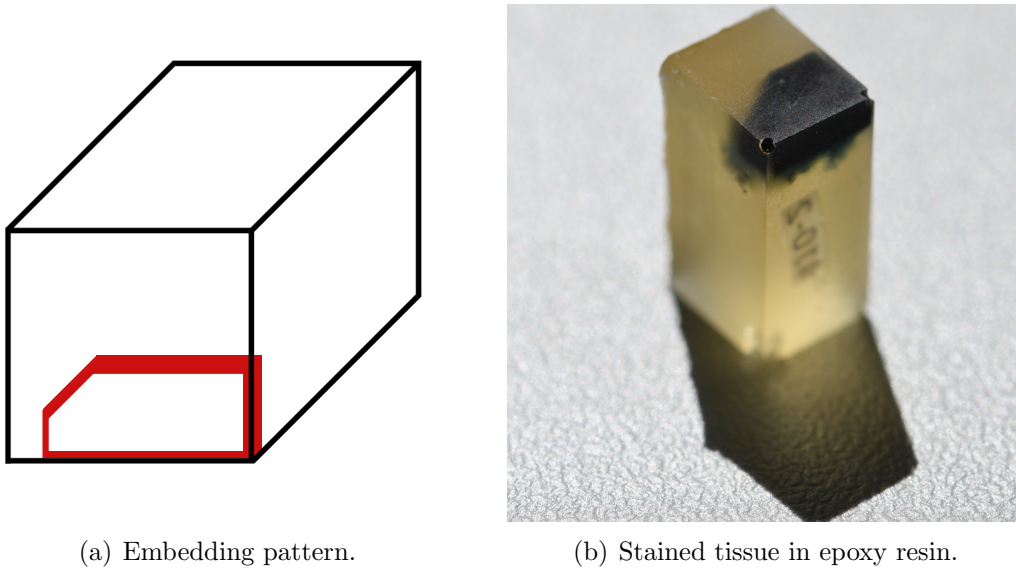


Figure 12: Embedding of tissue with the intimal layer facing forward in TAAB. (a) Schematic placement of tissue into the embedding form (block). (b) CB-stained aortic tissue embedded in TAAB resin with adventitial layer facing inward, hence the loose tissue.

2.4. Sectioning

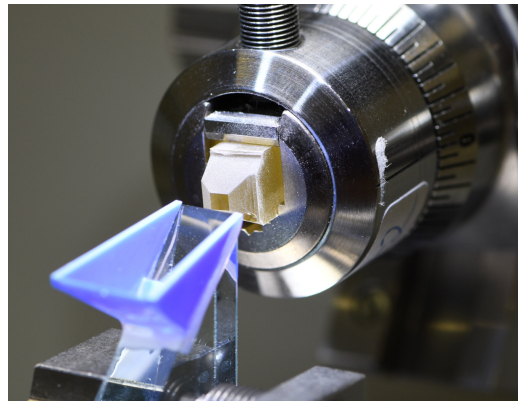
The embedding of the tissue in resin is a necessary step for cutting the sample with an ultramicrotome as depicted in Fig. 13(a). The principal work flow of preparing the specimen for investigation with a TEM are described in the following two paragraphs.

2.4.1. Microtome

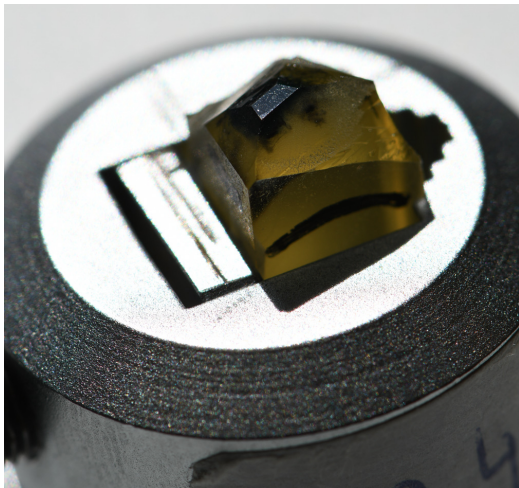
First the block is placed and fixed into a holder and trimmed with a trimming device or a razor blade to the edges of the tissue. The holder is then mounted into the microtome arm and a glass knife is fixed in front of the block-face, see Fig. 13(b) for semi-thin sectioning. This step is mainly for approaching the region of interest (ROI), in this work the specific layers, which then are prepared for ultra-thin sectioning. The microtome has an arm which describes a vertical movement, therefore the sample glides over a stationary knife. Each cycle, a section is cut by a precise movement of the arm towards the knife. To identify the position in the tissue the semi-thin sections are fished out of the water bath and dyed with a 1% toluidine blue solution to highlight certain structures observable under a light microscope. The specific embedding procedure implies reaching the intimal layer first, therefore it then is required to trim the block face even smaller, as in Fig. 13(c) and change the glass knife to a diamond knife to enable ultra-thin sectioning. The thickness of a section for TEM images are ~ 70 nm 13(d) and for recording tilt-series (1.4.2) it is common to take up 250 nm sections for greater z-dimension. Depending on the dimensions of the trimmed area a number of sections are then collected with a small copper grid, see Fig. 13(f) and the residual water is withdrawn with filter paper.

2.4.2. Stainer

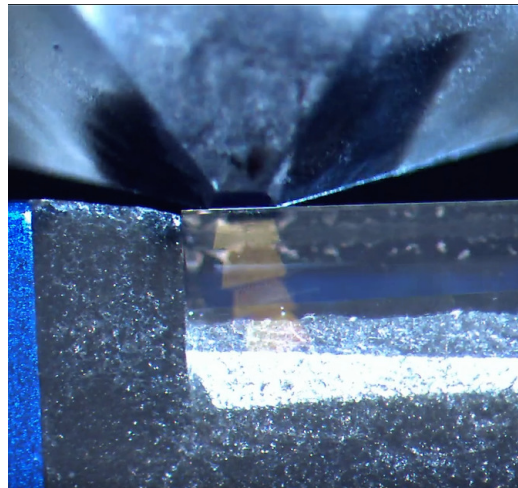
As described in section 1.4 the sections need to be stained with heavy metals to visualise the structures under a transmission electron microscope. Therefore the sections are stained with lead citrate and platinum blue for 7 minutes respectively 15 minutes in a Leica stainer. The staining protocol is done accordingly to standards in the lab and has multiple washing cycles. The duration of the complete staining process is 30 minutes. The residual water is again withdrawn with filter paper and the grids are put back into the grid box.

(a) Leica UC₇ ultramicrotome.

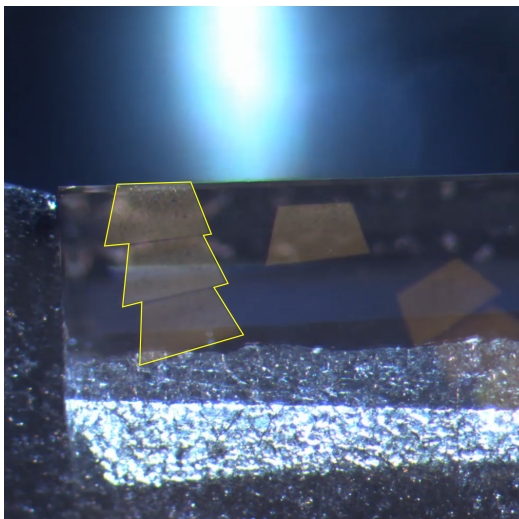
(b) Glass knife & mounted sample.



(c) Trimmed block (ultra-thin).



(d) Diamond knife & sections.



(e) Sections in water bath.



(f) Schematic grid with sections.

Figure 13: Sectioning work flow with Leica microtome. (a) Ultramicrotome with electric control (left). (b) Glass knife in front of a mounted trimmed sample in the microtome arm. (c) Desired region trimmed for ultra-thin sectioning. (d) Ultra-thin sections floating in the water bath of a diamond knife. (e) Marked sections to collect. (f) Schematic hexagonal grid (3 mm) with ultra thin sections (grey).

2.4.3. Fiducial Markers

For TEM tomography it is advised to use Fiducial Markers to enhance the alignment of the tilt series via feature tracking. The used protocol was described in paper [18]:359 and adapted in accordance to Guenter Resch, Nexperion:

1. Briefly vortex to resuspend gold colloid solution. For every five grids pipette 1.5 mL of gold colloid into a 1.5 mL microcentrifuge tube and pellet at maximum speed for 30 min.
2. During centrifugation place grids into grid support plate.
3. Remove half the supernatant, resuspend pellet by pipetting and sonicate in sonicating waterbath for 2 min.
4. Pipette solution onto grids until they are fully submerged in gold colloid.
5. Incubate for 10 min with gentle agitation and drop grid support plate onto a table to distribute the colloid evenly (approximately 10 cm).
6. Remove remaining gold solution with filter paper and rinse grids with ddH₂O.
7. Dry grids with filter paper and place back into the grid box.

The marked grids are then suited for tomography in TEM, hence the gold colloid is seen on each image therefore it should only be applied to the tomogram slices.

2.5. Transmission Electron Microscope

The Transmission electron microscope used is a FEI Tecnai G2 20 provided by the Medical University Graz. All images, tilt series and montages are done with SerialEM software and subsequently tilt series are processed with IMOD to generate tomograms. In the following section the basic configuration of a TEM for image and tilt series acquisition. First a montage, as in Fig. 14 depicted, is set up with "Set up full montage" in order to gather information distributed over the ultra-thin slices on the complete grid. Random spots on the slices are then searched for collagen structures and a magnification is chosen which allows determination of collagen fibrils and detects proteoglycans reliable.

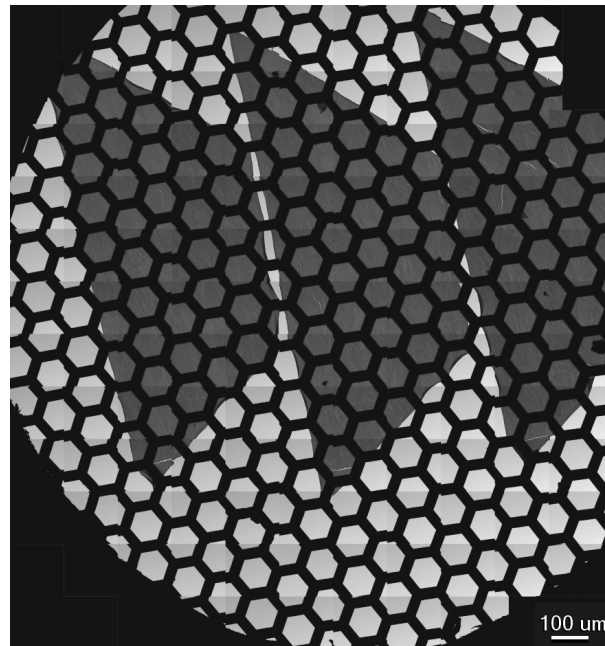


Figure 14: TEM-Map of grid with serial sections marked and made in SerialEM.

Between different magnifications the images of the transmission electron microscope has different rotation angles. Therefore it is crucial to work with a global coordinate system according to the orientation of the slide (axial/circumferential) which is set on the map by 2 points for each slide. On an image of a region of interest two distinctive spots are marked which are automatically added by SerialEM on the map, as can be seen later in chapter 3.2.2. By computing the angle between the vector in the global coordinate and the angle between the points on the images under different magnification the images can be put in relation regarding their orientation. This was realised by Anna Pukaluk in *MATLAB*[®].

For acquiring tilt series it is necessary to bake the ROI otherwise the drift of the section is too high to align images recorded at different angles. Therefore the beam is contracted and the magnification is set about 1500x to ensure that the whole area is baked. Afterwards the angles in both directions are checked by tilting the holder in "Tilt Control", seen in Fig. 15, during "View" modus till the grid blocks the image. These angles are written in the "Tilt Series Setup" and after checking all settings "Postpone" is selected, see Fig. 16, to re-examine all microscope settings before starting the tilt series.

For a general settings overview there is a step by step manual provided by SerialEM² and a video how to acquire a tilt series by BL3DEMC³ on youtube.



Figure 15: SerialEM tilt panel for tilting the grid.

The next step was the computation of a tomogram from the tilt series with IMOD-software. Although both collagen fibrils and proteoglycans were well depicted in the tilt series stack, the image data information in the tomogram was not suited for visualisation in *Amira*[®]. A mask for the proteoglycans was generated with the help of threshold operations in ImageJ-software. This mask enabled the segmentation of a proteoglycans surface with *Amira*[®]. Smoothing operations in ImageJ were chosen to increase the contrast between background and collagen fibrils for the "automated segmentation" in *Amira*[®]. The specific protocol used in ImageJ can be seen below.

```
run("Window/Level...");
run("Enhance Contrast", "saturated=0.35");
run("Apply LUT", "stack");
run("Close");
run("Median...", "radius=4 stack");
run("Subtract Background...", "rolling=20 disable stack");
run("Window/Level...");
run("Enhance Contrast", "saturated=0.35");
run("Apply LUT", "stack");
run("Close");
run("Unsharp Mask...");
run("Median...", "radius=5 stack");
run("Subtract Background...", "rolling=50 disable stack");
setAutoThreshold("Default");
//run("Threshold...");
setAutoThreshold("Default dark");
setAutoThreshold("Mean dark");
```

²https://bio3d.colorado.edu/SerialEM/hlp/html/about_tilt_series.htm

³<https://www.youtube.com/watch?v=xypelKFCacE>

```

setAutoThreshold("Default dark stack");
setOption("BlackBackground", false);
run("Convert to Mask", "method=Default background=Dark calculate black");
run("Close");

```

These image alterations were then saved and fed to *Amira*[®] where the new image stack was automatically segmented. Falsely assigned areas were deleted by hand with the help of the original tomogram image stack in the background leading to the final 3D visualisation.

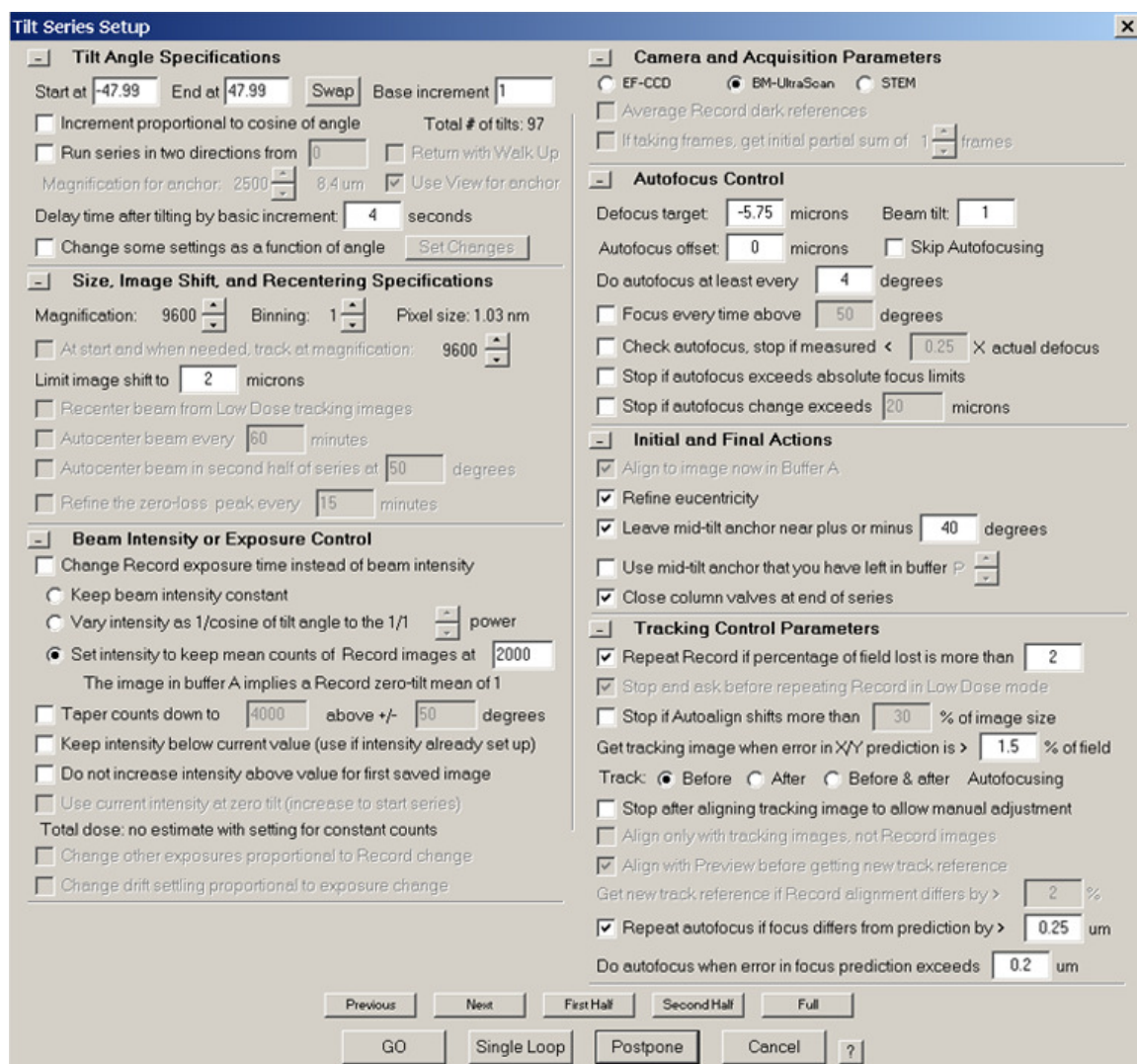


Figure 16: SerialEM tilt series setup for specification of the tilt series.

2.6. Test Data

The data obtained while testing is saved in an excel spreadsheet, with following entries:

- time [sec]
- Displacement 1 [mm]
- Force 1 [N]
- Displacement 2 [mm]
- Force 2 [N]
- Displacement 3 [mm]
- Force 3 [N]
- Displacement 4 [mm]
- Force 4 [N]
- Stretch 1-2 [-]
- Stretch 3-4 [-]
- Initial distance 1-2 [mm]
- Initial distance 3-4 [mm]
- No. of cycle [-]

The *displacement 1* denotes the change in x direction and the *displacement 2* in y direction.

In the course of this work the Cauchy stress was calculated according to a paper by Humphrey [10] using following formula.

$$\sigma_{11} = \lambda * \frac{F_1}{A} = \frac{F_1}{d * t} \quad (1)$$

d ... diameter [mm]

t ... thickness [mm]

A ... initial cross area [mm²]

F ... actual tension force [N]

σ ... stress [N/mm² = MPA]

λ ... stretch [-]

The Cauchy stress σ is calculated from the quotient of the actual extension force F and the initial cross section area A of the coin-shaped specimen multiplied by the stretch λ . Therefore the unit for the Cauchy stress is [mm²]. The axial and circumferential stresses were calculated and plotted with a *MATLAB*[®], see section 3.1 and appendix A.

3. Results

In this chapter results from the biaxial tests obtained from all samples (Table 2) and important preliminary results from the cutting and imaging steps for the first sample (Table 3) are presented. In total 6 human abdominal aortic tissue samples were investigated.

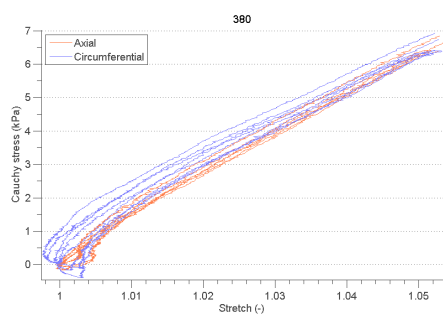
3.1. Biaxial Test

The biaxial testing data is plotted in this paragraph for each stretch of the sample number 380, see Figures 17, 18, 19. The testing results for the other samples, see Tab.3 are attached in the section Appendix A.

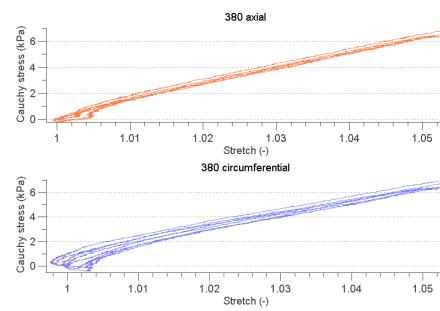
For each test the data is plotted into one diagram, then splitted into axial and circumferential direction data, at least one preconditioning cycle is plotted and the measuring cycle is also plotted for each stretch. Due to saving errors during testing, there is no measuring cycle for the 5% stretched 386 specimen (= No. 386-2), the same happened to the preconditioning cycle for the sample No. 417-2.

Table 2: Biaxial testing samples.

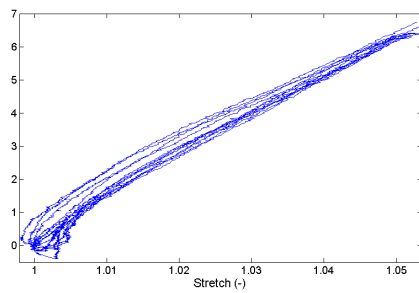
Sample	Stretch					TEM Nr.	plaques
1	0%	5%	10%	15%		380/1-4	no
2	0%	5%	10%	15%	20%	386/1-5	no
3	0%	5%	10%	15%		386/1-4	no
4	0%	5%	10%			417/1-3	yes
5	0%	1%				418/1-2	yes
6	0%	5%	10%	15%		432/1-4	yes



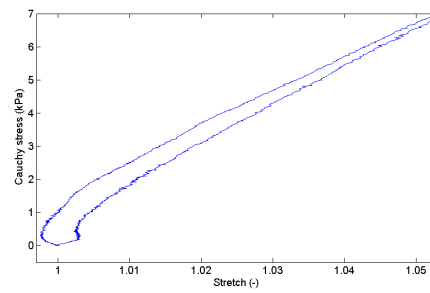
(a) Plot of all 5% cycles.



(b) Separate graphs for all cycles.

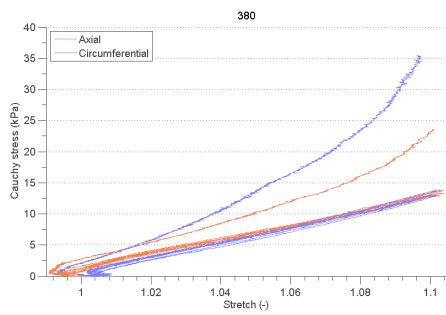


(c) Preconditioning.

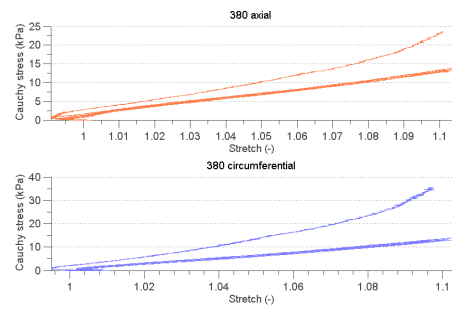


(d) Measuring cycle.

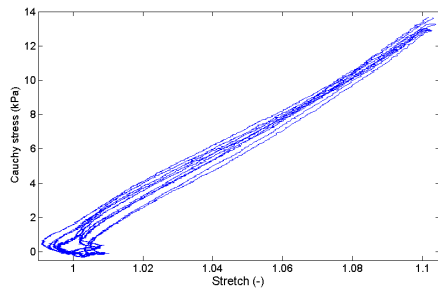
Figure 17: Biaxial testing plots for 380-2 sample at a stretch (λ) of 1.05.



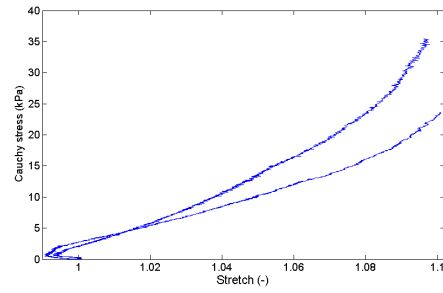
(a) Plot of all 10% cycles.



(b) Separate graphs for all cycles.

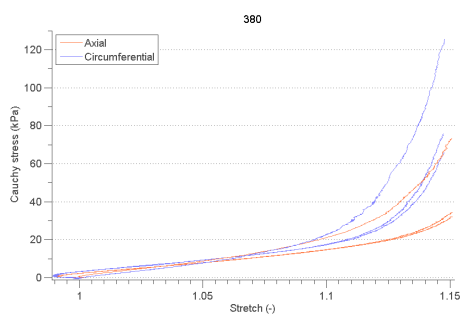


(c) Preconditioning cycles.

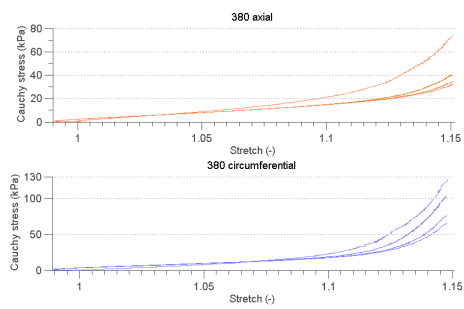


(d) Measuring cycle.

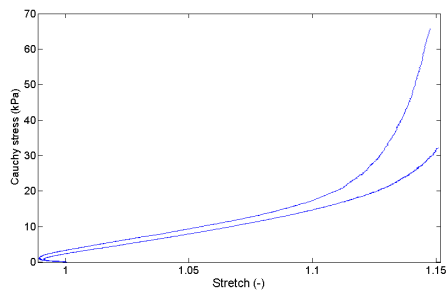
Figure 18: Biaxial testing plots for 380-3 sample at a stretch (λ) of 1.1.



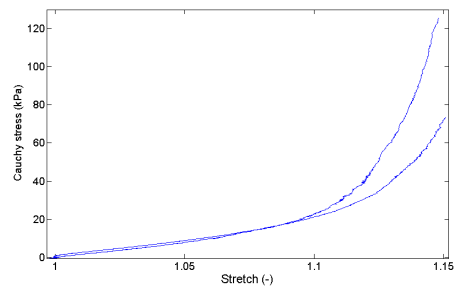
(a) Plot of all 15% cycles.



(b) Separate graphs for all cycles.



(c) Preconditioning cycles.



(d) Measuring cycle.

Figure 19: Biaxial testing plots for 380-4 sample at a stretch (λ) of 1.15.

3.2. Ultrastructural Investigation

The preliminary results in this paragraph are presented for understanding the embedding process and for a better connection between macroscopic and nanoscopic scale. All available sections and TEM results are listed in Table 3, with following entries: intimal (I), medial (M), adventitial (A) layers, tomogram (TOMO) and amira reconstruction (3D).

Table 3: Complete work flow with sample No 1.

TEM Nr.	Section			TEM	TOMO	3D
380-1		M	A	M	M	M
380-2	I	M	A	M		
380-3	I	M	A	M		
380-4	I	M	A	M		

3.2.1. Light Microscope Images

In this paragraph in-plane sections of each layer (except intimal layer for 380-1) under different stretches acquired during sectioning 2.4 are shown. All images are recorded at a Leica DM6000 B light microscope with a Olympus DP72 camera. Structural and saturation differences are addressed in the section Discussion 4.

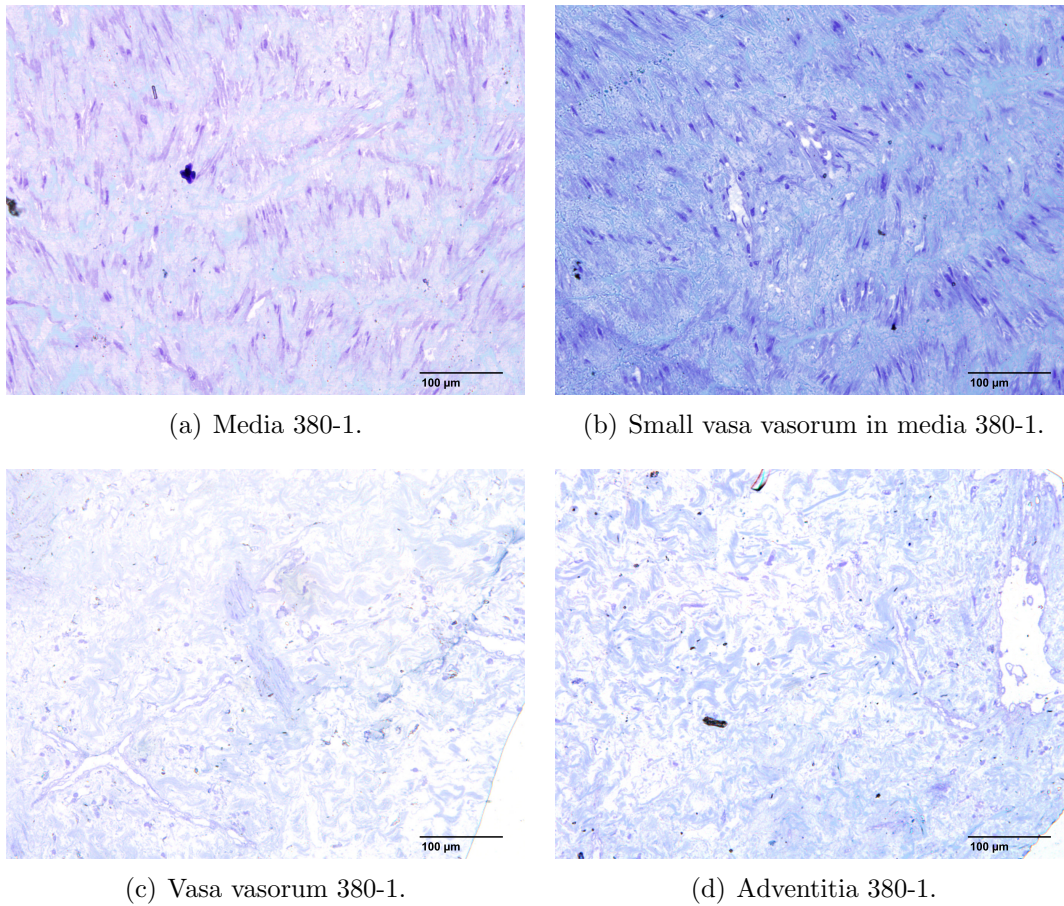


Figure 20: Light microscope images of 380 specimen without stretch dyed with toluidine blue solution (Magnification: 20x). (a) Image of the medial layer near to intima (IEL). (b) Medial layer with with small vasa vasorum . (c) Adventitia near external elastic lamina. (d) Adventitial layer with some wrinkles (transparent black lines). Scale Bars 100 μm.

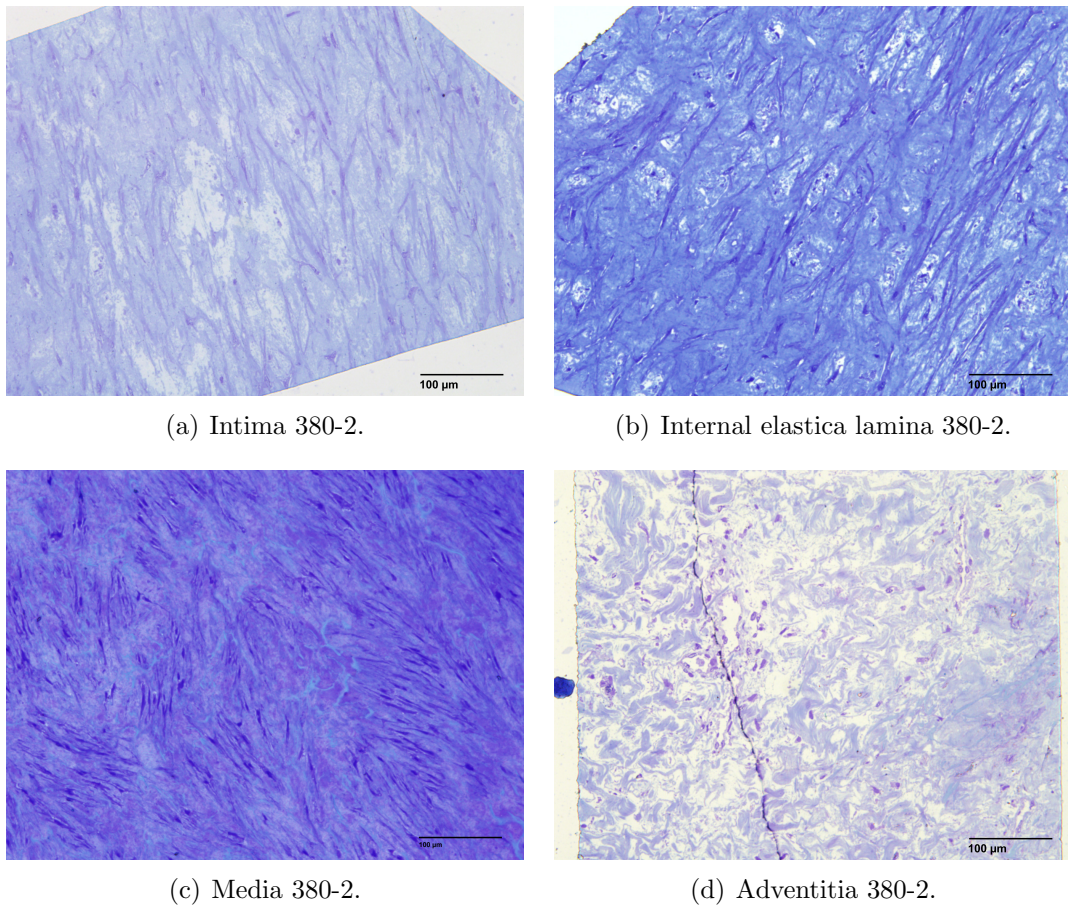


Figure 21: Light microscope images of 380 specimen under 5% stretch dyed with toluidine blue solution (Magnification: 20x). (a) Ultra-thin trimmed section of the intima. (b) Image of the internal elastica lamina with denser structures. (c) Medial layer with distinct light blue structures. (d) Section of the adventitia with structural demarcated space, which are vasa vasorum. Scale Bars 100µm.

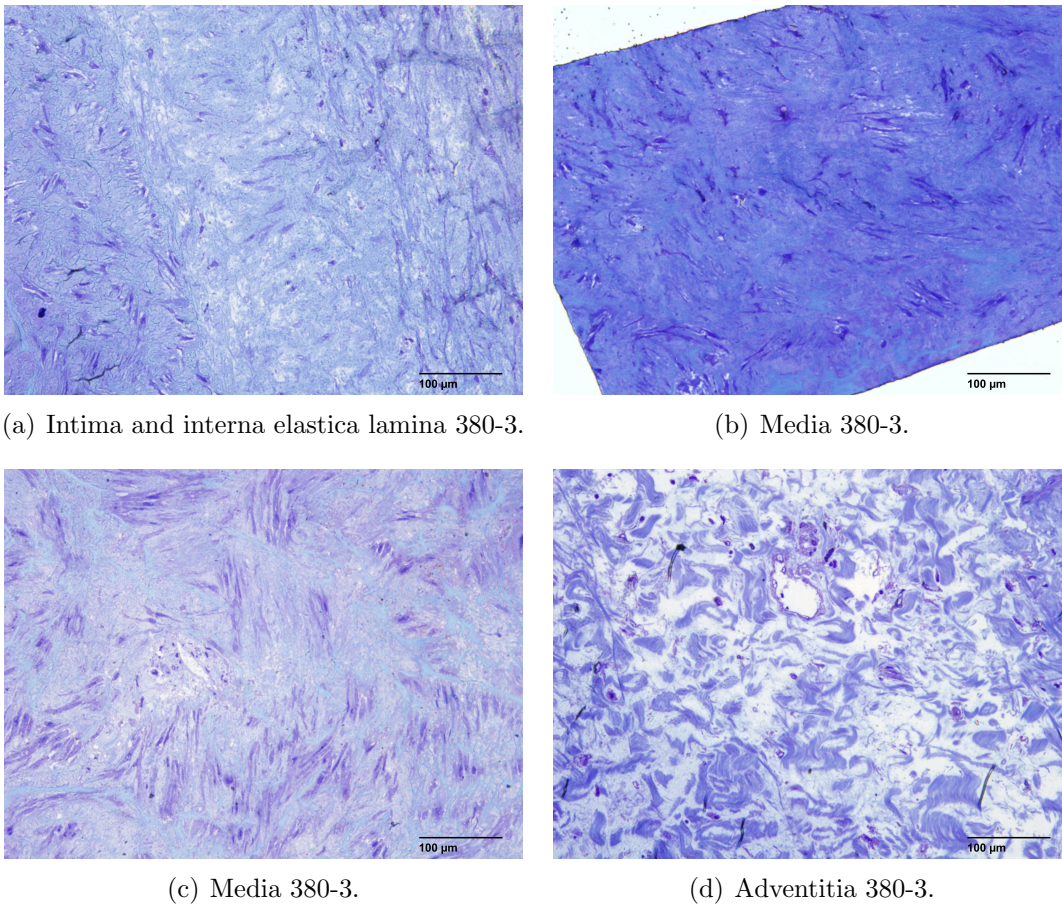


Figure 22: Light microscope images of 380 specimen under 10% stretch dyed with toluidine blue solution (Magnification: 20x). (a) Section with intima in the middle part of the image. (b) Image of the medial layer near to intima. (c) Section of the media with vasa vasorum. (d) Adventitial layer with some wrinkles (transparent black lines). Scale Bars 100 μm.

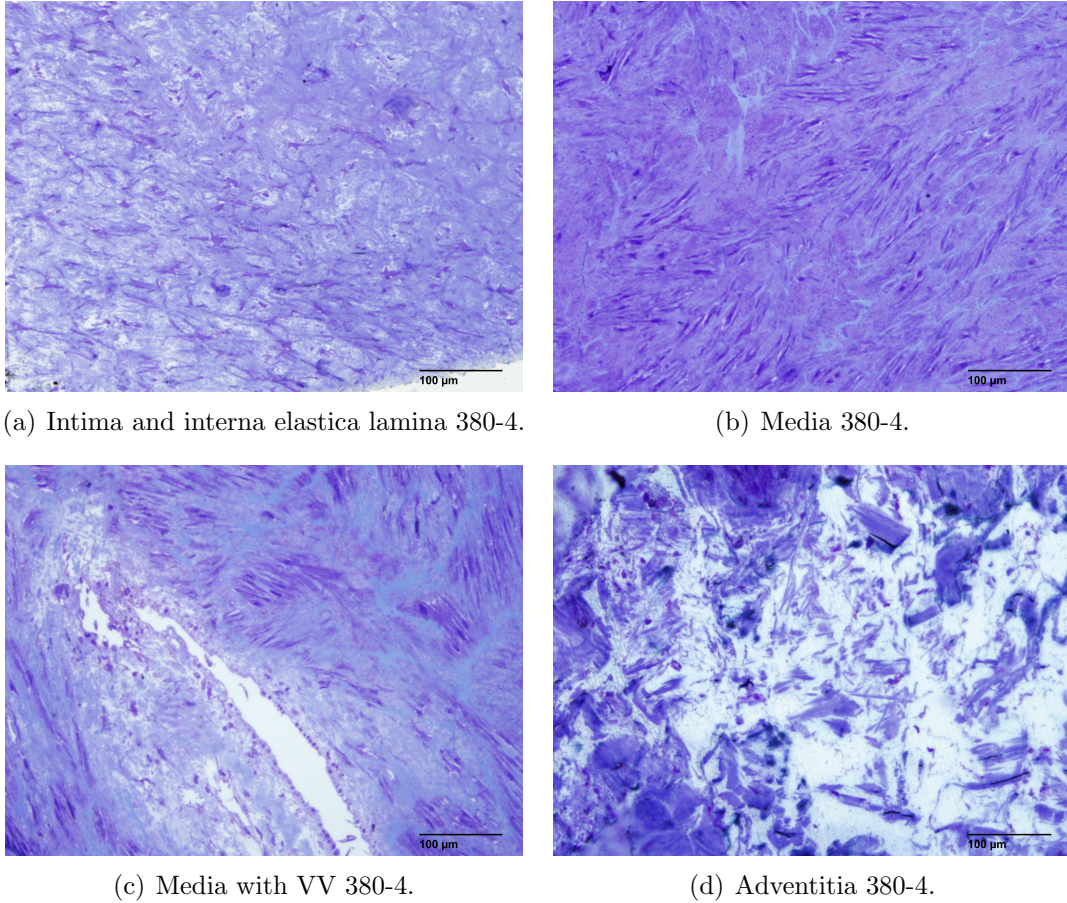


Figure 23: Light microscope images of 380 specimen under 15% stretch dyed with toluidine blue solution (Magnification: 20x). (a) Section of the intima with starting of structural changes on the left side (IEL). (b) Image of the medial layer with dense structure.(c) Section of the media with a big vasa vasorum. (d) Adventitia with blurry edges because of air bubbles between section and microscope slide. Hence spaces between structures. Scale Bars 100μm.

3.2.2. TEM Image Acquisition

The images in this paragraph are in order of the work flow at the TEM. Only a representative selection of acquired maps and images are presented in this work.

The map in Fig.24 displays the three medial layer sections of a 5% stretched sample with the investigated points (red small crosses). In Figures 25, 26 and 27 long structures are collagen and the black dots throughout the image are staining artefacts. Proteoglycans are visible as small elliptical shapes perpendicular to the collagen fibres in Figures 26 and 27.

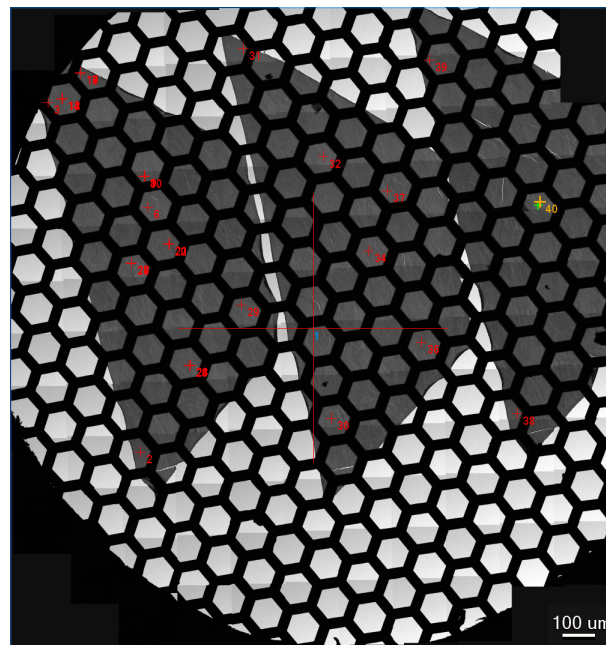


Figure 24: TEM map of the 380-2 medial layer with marked investigated points. Magnification: 96x.

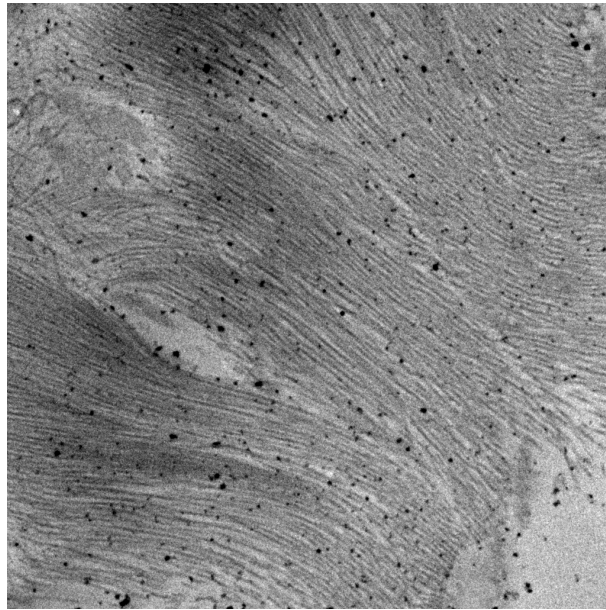


Figure 25: TEM image of medial layer 380-1 Magnification: 1650x.

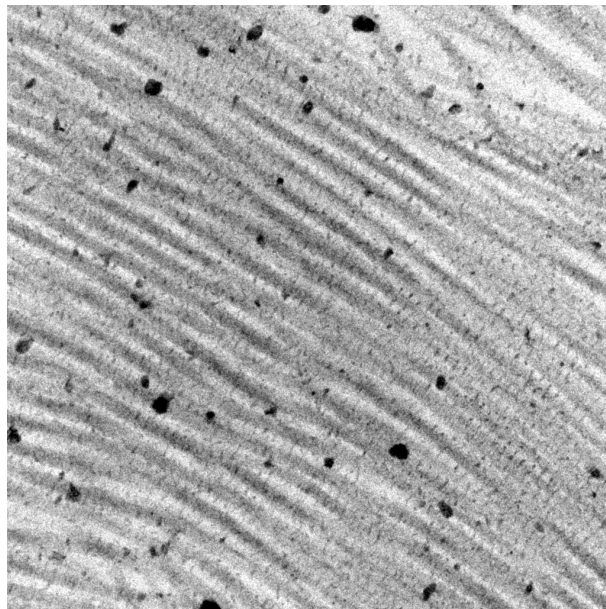


Figure 26: Zoom in TEM image of image in Fig.25. Magnification: 12500x.

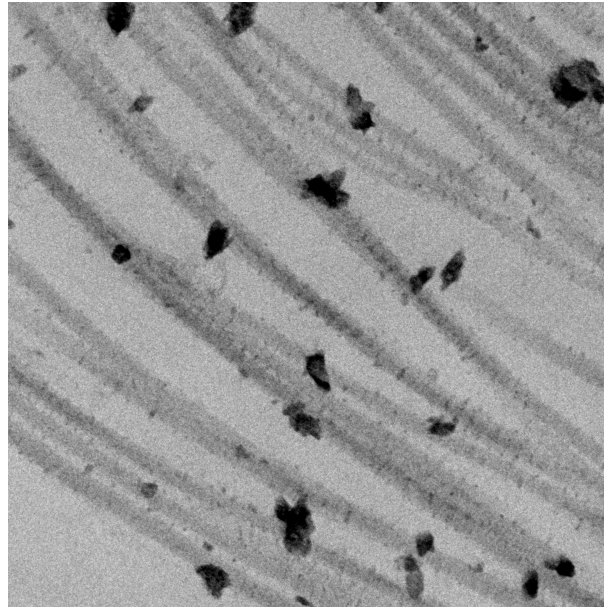


Figure 27: TEM image of medial layer 380-1 Magnification: 15000x.

EDX Acquisition

Additionally elemental analysis graph with Energy-dispersive X-ray spectroscopy (EDX) of the staining artefacts in Fig.27 can be seen in Fig.28.

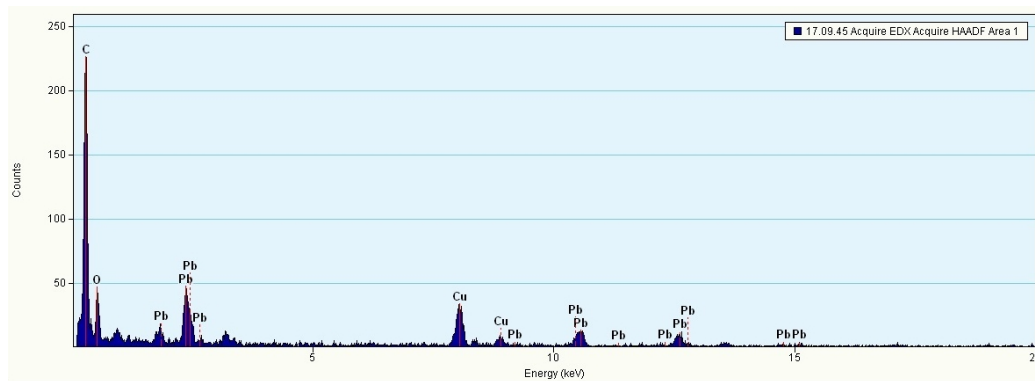


Figure 28: EDX spectrum of one precipitation on TEM image in Fig.27 .

3.2.3. Tilt Series Acquisition

In Fig.29 one image of the recorded tilt series with 121 tilts is shown. In accordance to the TEM images the long structures are collagen fibrils and the proteoglycans can be seen as small elliptical shaped structures.

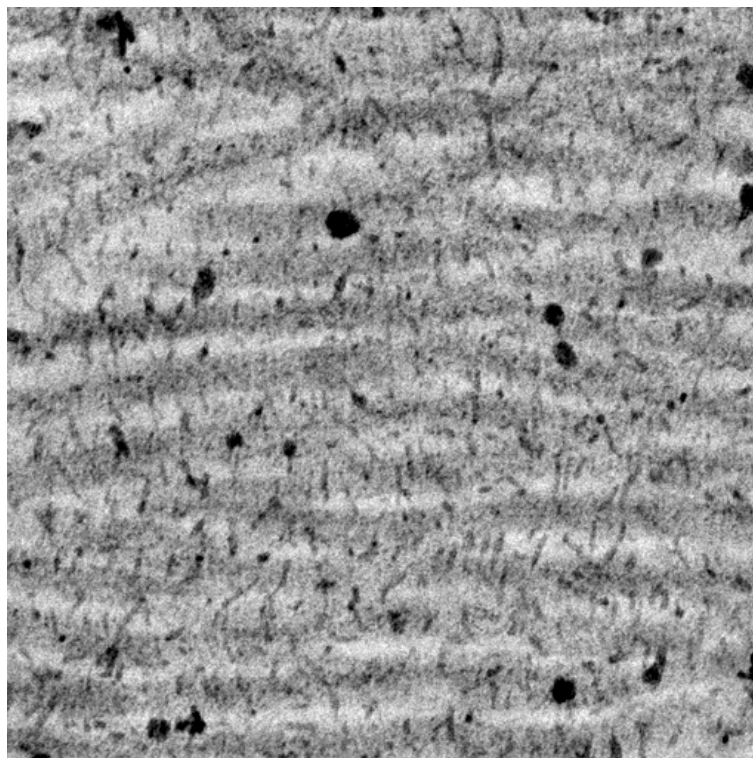


Figure 29: Image from the tilt series at 1° tilt angle. Magnification: 19000x

3.2.4. Tomogram

One slice of the tomogram generated with IMOD software can be seen in Fig.30. The complete tomogram has 100 slices in the z-direction and 2048 both in x- and y-direction.

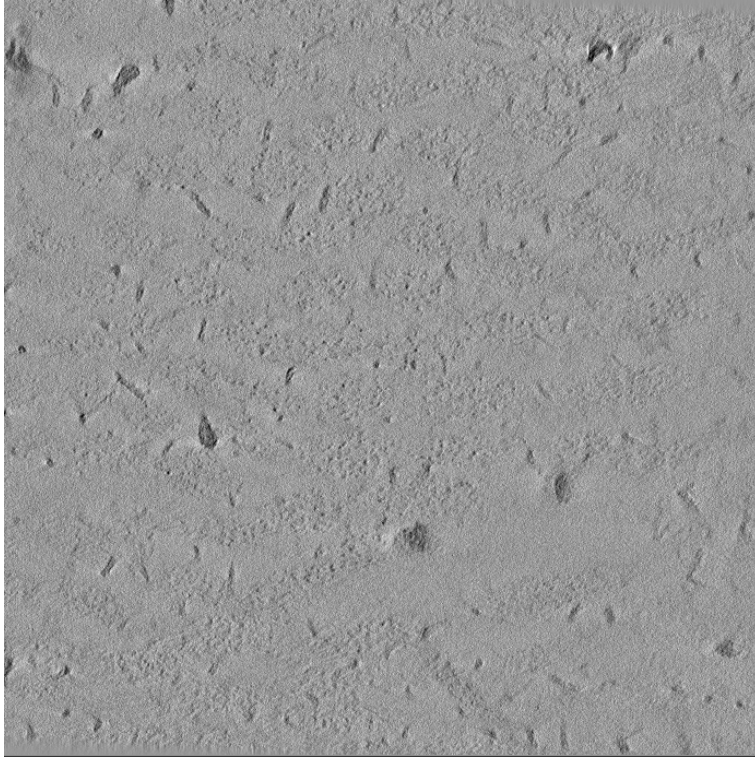


Figure 30: One slide of the tomogram stack computed with IMOD.

3.2.5. 3D-Amira[®] Reconstruction

For the 3D reconstruction in *Amira*[®] one slide of the proteoglycan-mask is shown in Fig.31, which is then taken to generate the proteoglycan surface (blue) with *Amira*[®] as in Fig.32. The final segmentation of collagen fibrils (red structures) for one slide can be seen in Fig.33.

The reconstruction in Fig.34 shows the collagen fibrils in red and the proteoglycans in blue in front of one slide of the tomogram. The orange lines hint the level of the selected slice in the tomogram. To give a better three dimensional view, the mesh is tilted and there is no background slide only the y- and z-plane tomogram slides are inserted in Fig.35.



Figure 31: One slide of a mask generated with ImageJ for visualising proteoglycans.

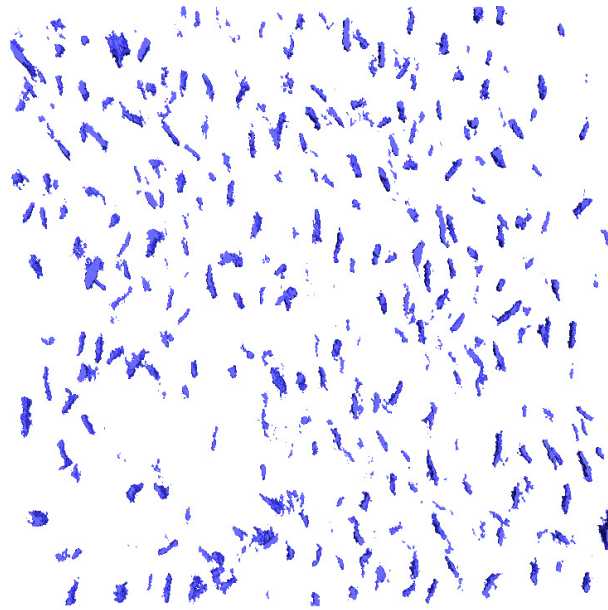


Figure 32: 3D *Amira*[®] surface of the proteoglycans generated from the mask above.

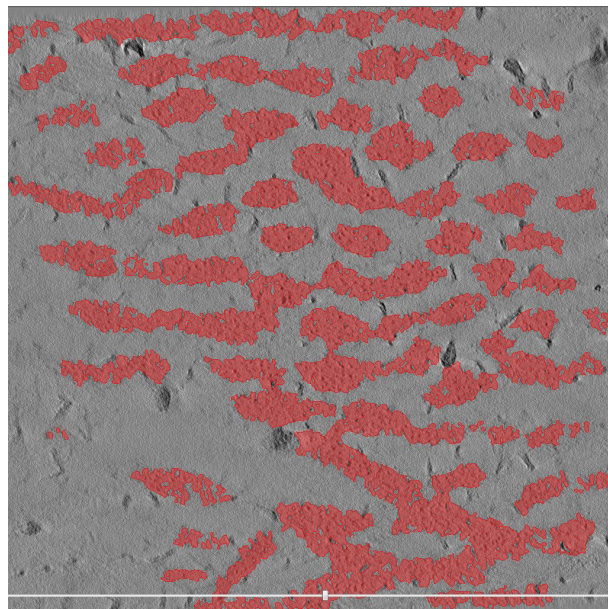


Figure 33: Final segmentation of collagen fibrils on slide 50 after image processing of the tomogram stack.

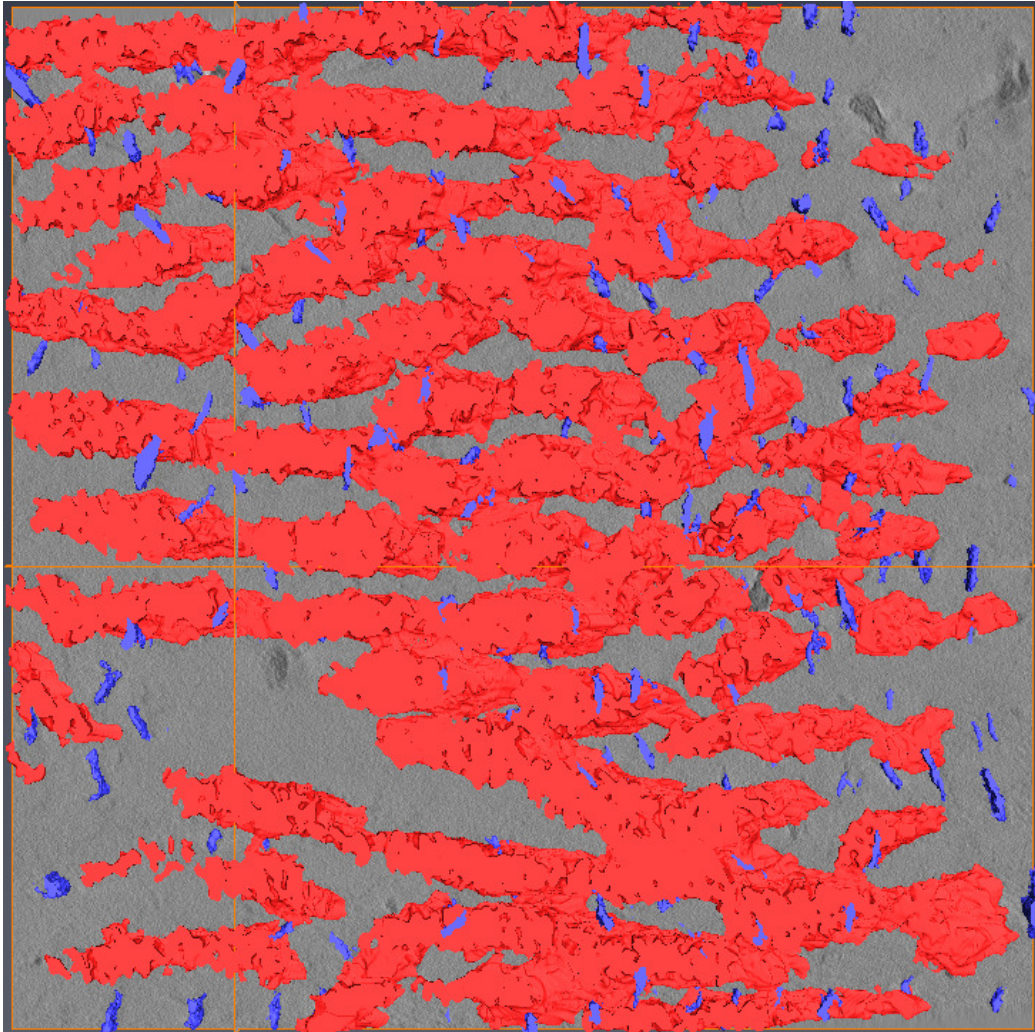


Figure 34: *Amira*[®] 3D-Visualisation with tomo slice Nr.50 as background.

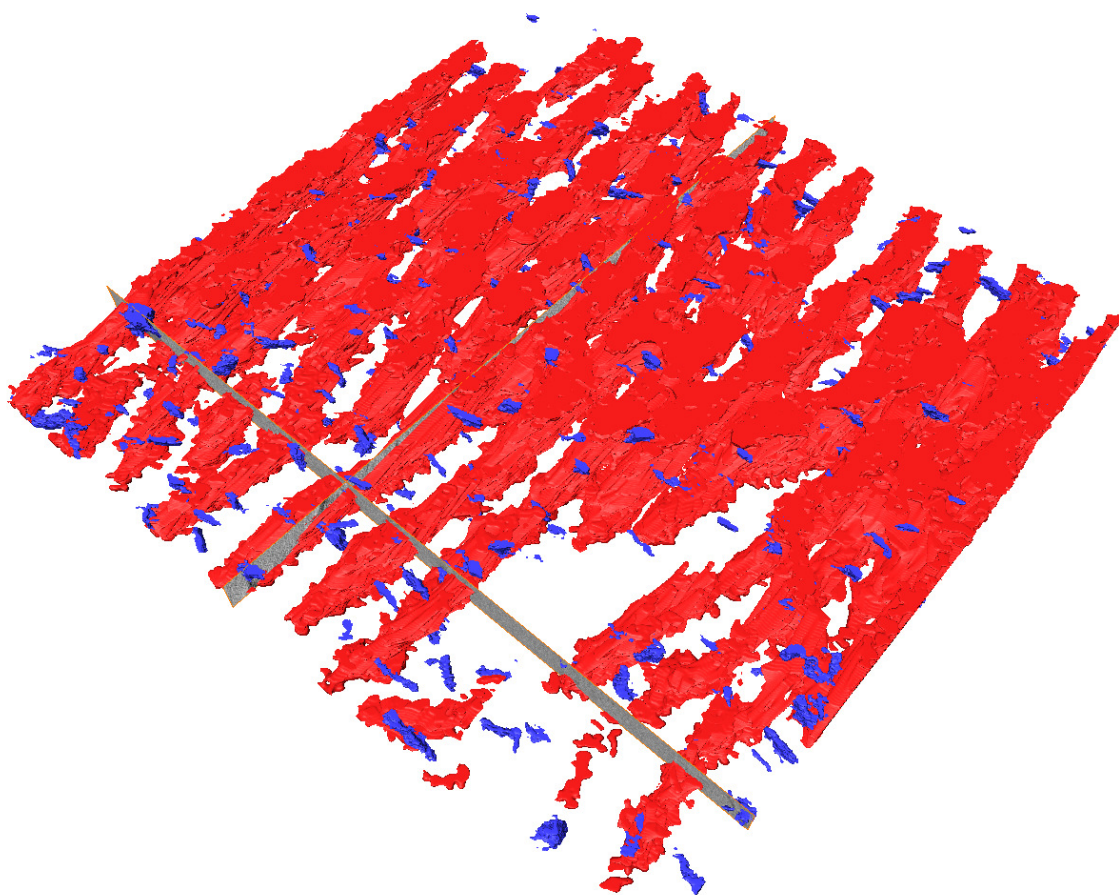


Figure 35: Tilted 3D-Visualisation with *Amira*[®].

4. Discussion

The aim of this thesis is to implement a work flow starting with fixating biaxial stretched human abdominal aortic tissue and investigate the effects at the ultra-structural level with transmission electron microscopy.

To lower experiment costs the basin for fixating the specimen under stretch in glutaraldehyde was redesigned to reduce the amount from 5 l to 0.75 l per stretch test. Second the costs were significantly lowered by choosing a micro well plate to incubate the specimen in Cuproline Blue. This section evaluates the findings which occurred during the implementation of the methods and analyses the preliminary results as well as the final tomogram, in respect to future work in this project.

The plotted data from biaxially testing the specimen are mostly as expected. The results nicely display the difference between low and high stress response, see Fig. 17(a) and Fig. 19(a). The 5% stretches are solely in the elastic domain which can be explained due to the fact that collagen bundles are undulated structures which are firstly straightened under stretch. Therefore their contribution is only seen at higher stresses. Aortic tissue is stiffer in the circumferential direction which is depicted by each plot except in Fig. 40 where it is the other way around. This may be due to the elastic stress response in low stress regions. The necessity of preconditioning is clearly observable at the higher stresses, except at the sample tested last. It was reported that one of the load cells were found to be corrupted afterwards, this might be the reason for this exception.

The most difficult step whilst testing the specimens with the biaxial testing device was exposing the specimen with a uniform pre-load. This can be seen in almost any plots, hence the seemingly reduction of the specimen diameter, recorded by the camera. The effort to rope the specimen into the device as evenly as possible, to avoid out of plain stretching likely challenging. It is of uttermost importance to find a better solution going forward.

Regarding the atherosclerotic tissue it was observable that the testing approach needs to be reviewed. First of all it was not easy to find a large enough spot of the tissue to test without a plaque, secondly it was sometimes the case that a plaque wasn't visible. Therefore it was discovered whilst hooking the specimen and once (432-3) even later when cutting it into smaller pieces for embedding. The heavy atherosclerotic tissue could not be stretched anywhere near the desired amount, as can be seen

in Tab.2, which would be needed for comparison. It may be a possibility to address this issue by adding a 2% stretch test to the procedure instead of the 20%, hence autolysis of human tissue after death. The specimen size was also an issue because of simultaneous analysing structures on the ultra-structural level with TEM and on the microscopical with second-harmonic imaging microscopy (SHIM) based on second harmonic generation (SHG). Therefore it might be needed to lower the different amounts of stretches, for example to 0%, 2%, 5% and 10%.

The effects of residual stresses in aortic tissue have to be considered although the used embedding protocol is standard in the laboratory. The challenge of in-plane sectioning starts with correctly aligning to the tissue surface and involves non concentric growth of the individual layers, as best observable in Fig. 22(a), where it is obvious that the section contains more than one layer despite careful alignment. Bad aligning is the reason for no light microscope image of the intimal layer under no stretch (380-1). During first sectioning there were no references to compare the stained sections to. Only the vasa vasorum, as displayed in Fig. 22(b) hinted a structural change. These vasa vasorum increase their lumen towards the outer most layer, as can be seen in all the light microscopy images of the each stretch value (Figures 20, 21, 22, 23). The apparent saturation differences in all light microscopy images are due to pH concentration within the tissue, structural/histological differences and thickness of the sections which are dyed with 1% toluidine blue and therefore weren't removed with white balancing methods or other image processing tools. Some layer specific features could be defined for future sectioning of aortic tissue: the intimal layer has long nearly parallel structures, only sections of the media have these completely saturated light blue (cyan blue) structures and last but not least in the adventitial layer wavy structures which seem to be collagen bundles are separated by structures which are not stained by toluidine blue. To definitely determine the structures which are dyed, slices have to be dyed by specific antibodies, hence TAAB resin doesn't allow most antibodies to infiltrate the tissue. To evaluate the dimensional distances between the different stretches more data needs to be collected but judging the difference between Fig. 20(d) and Fig. 23(d) the distance between the assumed collagen bundles seem to widen with increased stretch values. Further the vasa vasorum in Fig. 23(c) could either indicate a "lucky" sectioning position or an effect of fixating the tissue under 15% stretch, as mentioned there is more data needed for a significant statement. Additionally in Fig. 21(b) the internal elastica lamina is displayed which

shows both structural similarities to intima in Fig. 21(a) and media in Fig. 21(c). SerialEM has proven to be indispensable for this project regarding acquiring tilt series, computing the mean fibril orientation due to the image rotations under different magnifications and is also helpful to keep an overview which regions were already observed as is illustrated in the exemplary map in Fig. 24 of a medial layer under 5% stretch. Randomly chosen spots on the slice are searched for collagen fibrils, as can be seen in Fig. 25, after significantly zooming in the CB dyed proteoglycans can be observed as elliptical structures in Fig. 26. Another magnification step higher reveals interfibrillar proteoglycans and demonstrates the use of tomography to estimate the relation between collagen fibres and proteoglycans. To determine the cause of the apparent staining artefacts, EDX spectroscopy was chosen to analyse the precipitation seen in Fig. 27. The EDX spectrum, shown in Fig. 28 identified lead as the main contamination on the sample. After staining our samples together with other tissue, which then wasn't affected, further validation is necessary to determine whether interactions between chemicals used during the embedding protocol (especially CB and UA) or our sample itself causes these precipitation.

Embedding, sectioning and transmission electron microscopy are all time consuming procedures therefore only one specimen is prepared for ultrastructural investigation, thus there is no conclusive statement regarding the effects of different extension on the nano-scale of tissue yet.

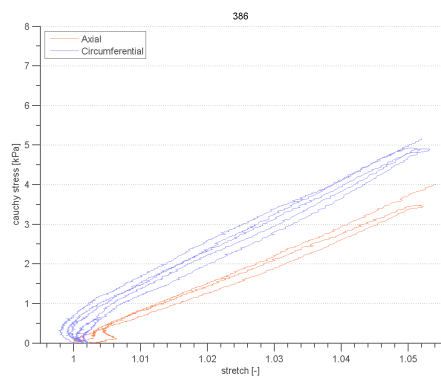
The computation of the tomogram from a tilt series with IMOD without fiducial markers generated a drift to the right side of the image stack, see Fig. 35. It is believed that the better feature tracking with fiducial markers would minimise this effect. By comparing Fig. 34 and Fig. 35 the extend of the afore mentioned effect can be estimated.

Although both collagen fibrils and proteoglycans are well depicted in the tilt series stack, as seen on the slide in Fig. 29 the image data information in the tomogram, compare Fig. 30 is not suited for visualisation in *Amira*[®]. After several attempts in *Amira*[®] it was chosen to generate a mask with threshold operations in ImageJ-software for the proteoglycans. This mask enabled the generation of the pretty accurate surface of proteoglycans with *Amira*[®].

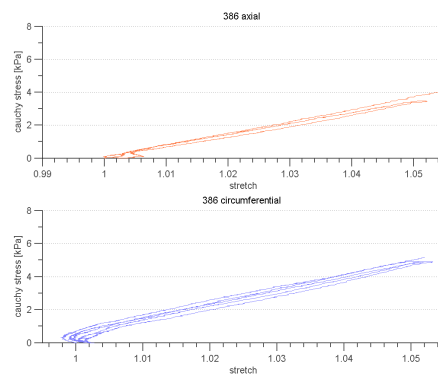
Similar approaches for the collagen fibrils did not turn out successful, therefore smoothing operations in ImageJ were chosen to increase the contrast between background and collagen fibrils for the "automated segmentation" in *Amira*[®] where areas

which were wrongly added to the collagen have been deleted by hand with the help of the original tomogram data in the background for each slide, as depicted on one slide in Fig. 33. This slow and repetitive task could be significantly shortened by using fiducial markers, by post processing the tilt series image stack and tomogram data in the future.

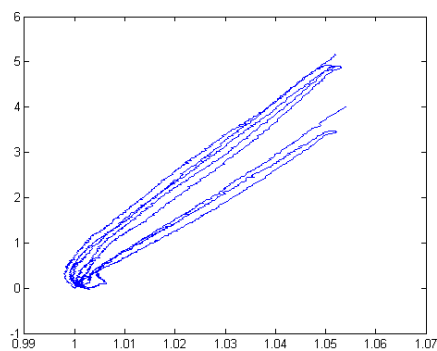
A. Testing Data Plots



(a) Plot of all 5% cycles.

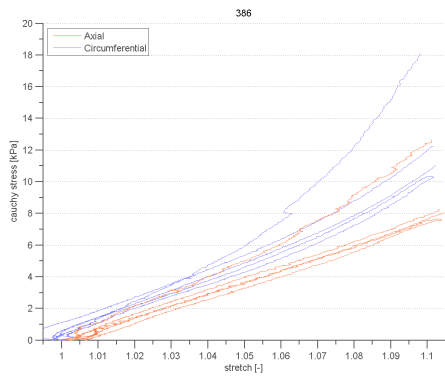


(b) Separate graphs for all cycles.

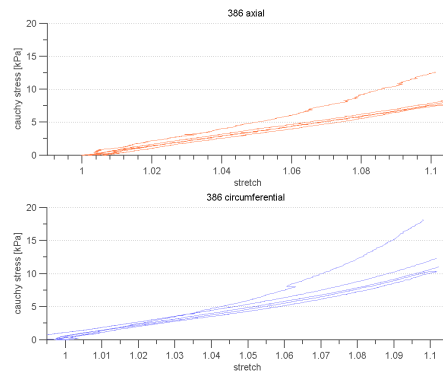


(c) Preconditioning.

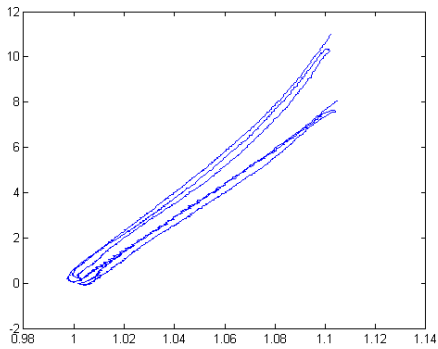
Figure 36: Biaxial testing plots for 386-2 sample.



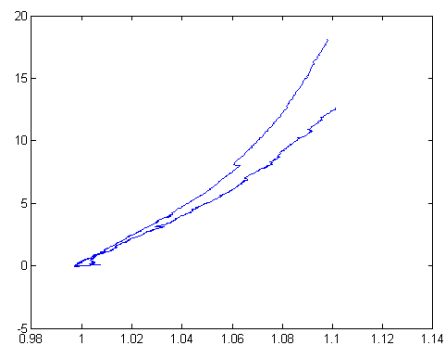
(a) Plot of all 10% cycles.



(b) Separate graphs for all cycles.

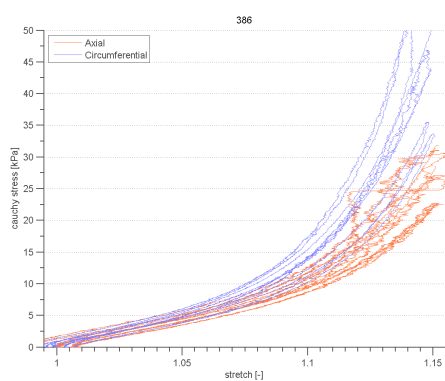


(c) Preconditioning cycles.

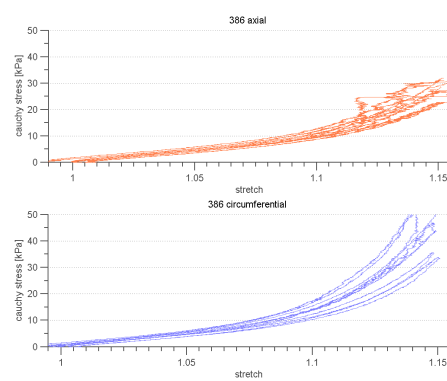


(d) Measuring cycle.

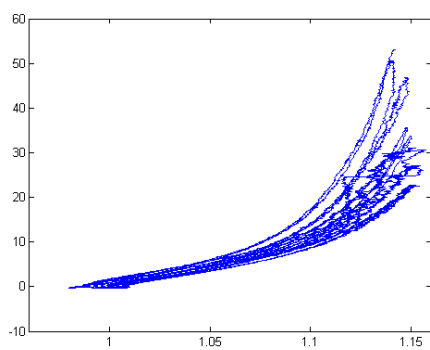
Figure 37: Biaxial testing plots for 386-3 sample.



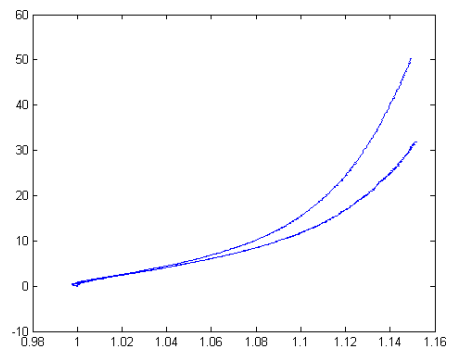
(a) Plot of all 15% cycles.



(b) Separate graphs for all cycles.

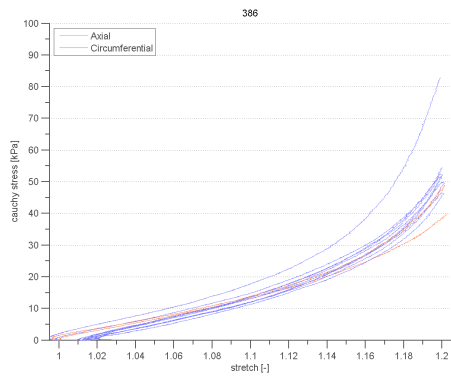


(c) Preconditioning cycles.

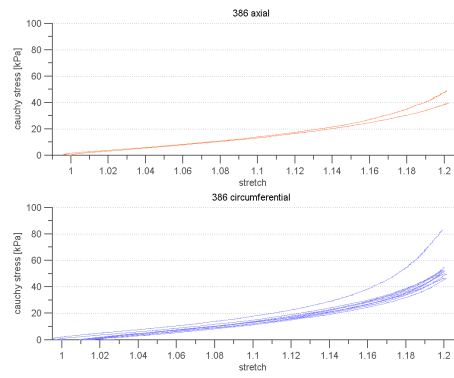


(d) Measuring cycle.

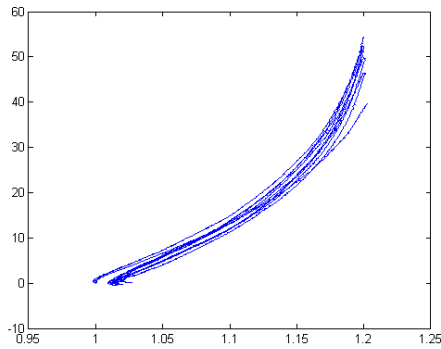
Figure 38: Biaxial testing plots for 386-4 sample.



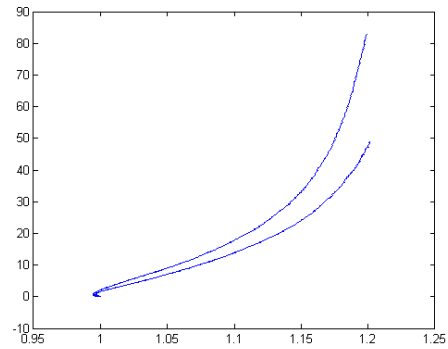
(a) Plot of all 20% cycles.



(b) Separate graphs for all cycles.

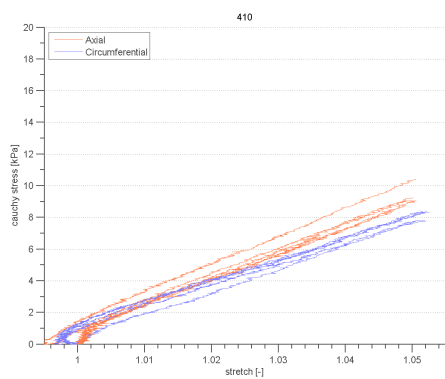


(c) Preconditioning cycles.

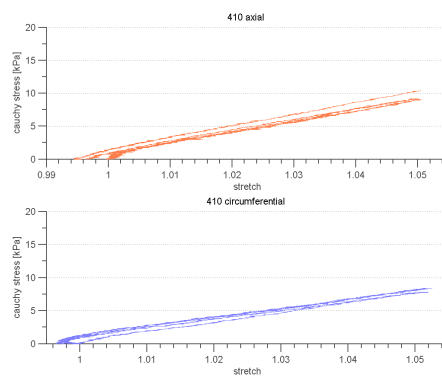


(d) Measuring cycle.

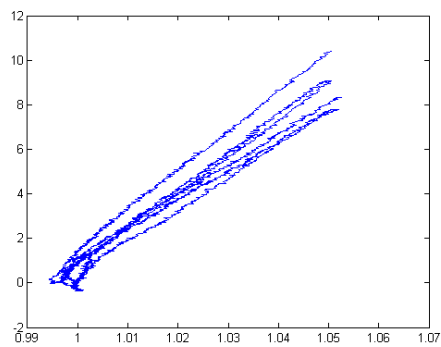
Figure 39: Biaxial testing plots for 386-5 sample.



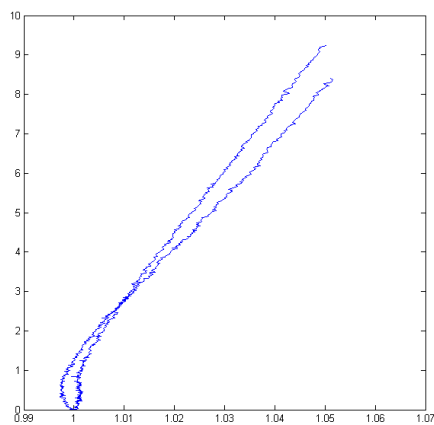
(a) Plot of all 5% cycles.



(b) Seperate graphs for all cycles.

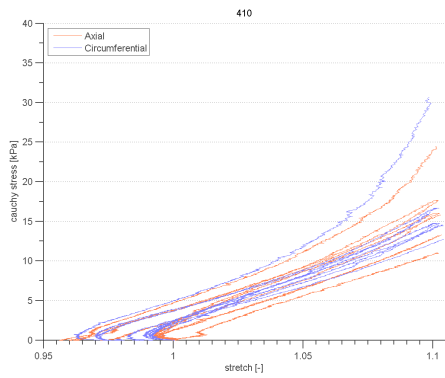


(c) Preconditioning.

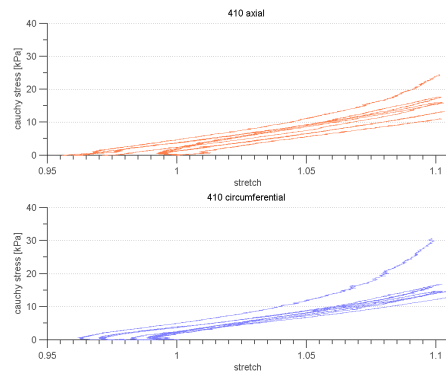


(d) Measuring cycle.

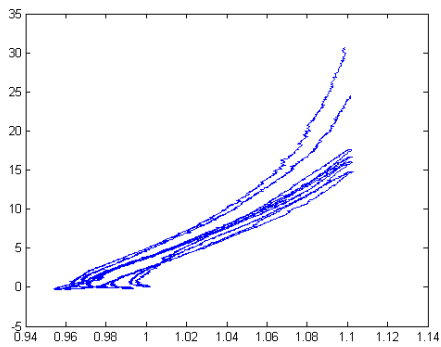
Figure 40: Biaxial testing plots for 410-2 sample.



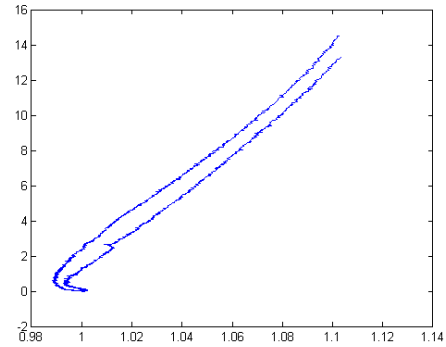
(a) Plot of all 10% cycles.



(b) Separate graphs for all cycles.

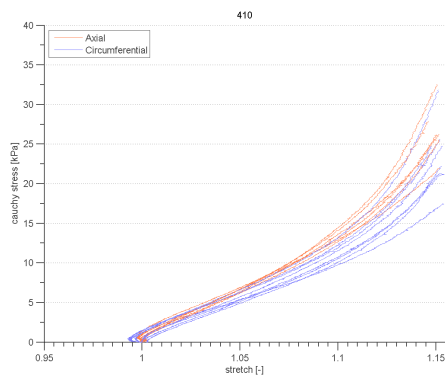


(c) Preconditioning cycles.

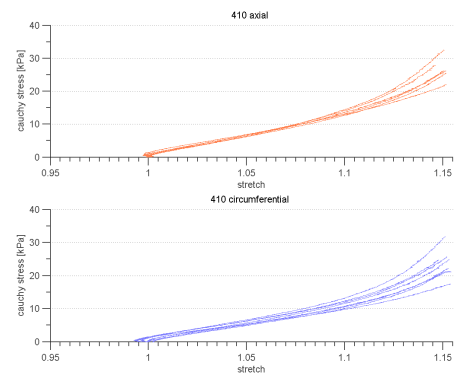


(d) Measuring cycle.

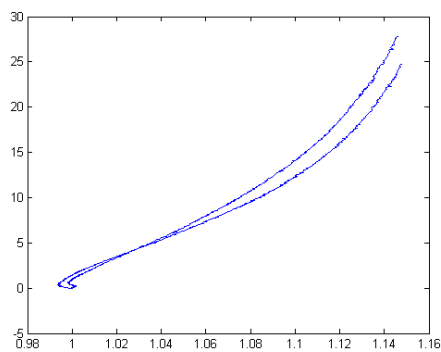
Figure 41: Biaxial testing plots for 410-3 sample.



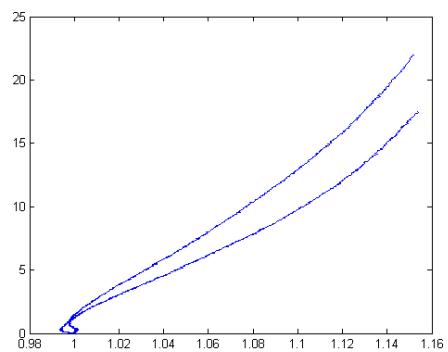
(a) Plot of all 15% cycles.



(b) Separate graphs for all cycles.

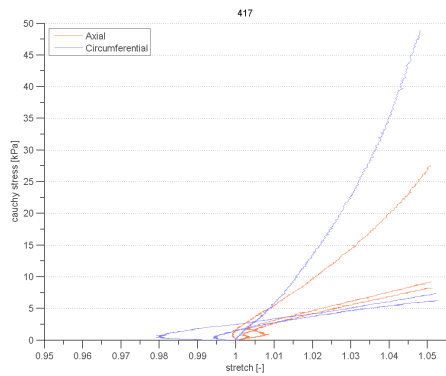


(c) Preconditioning cycles.

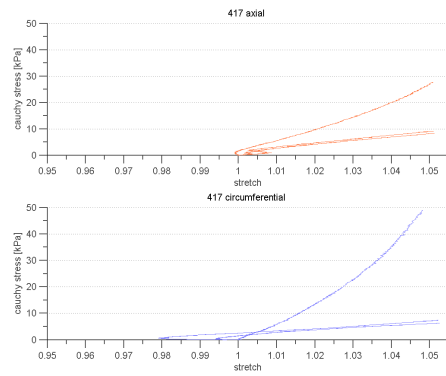


(d) Measuring cycle.

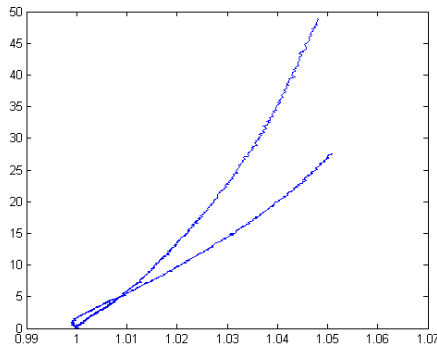
Figure 42: Biaxial testing plots for 410-4 sample.



(a) Plot of all 5% cycles.

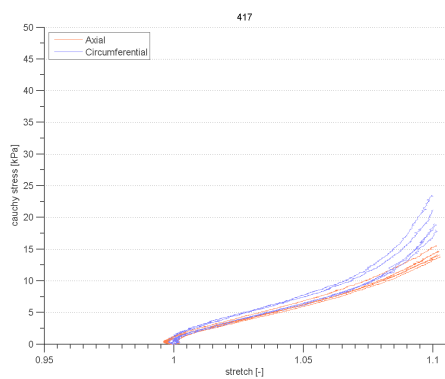


(b) Seperate graphs for all cycles.

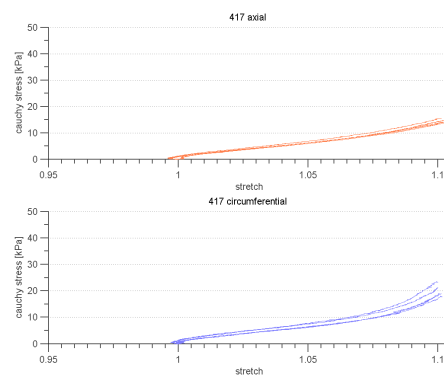


(c) Measuring cycle.

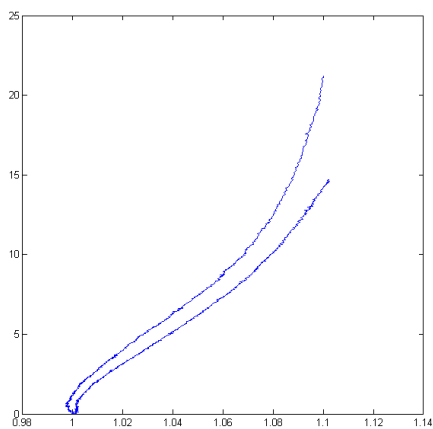
Figure 43: Biaxial testing plots for 417-2 sample.



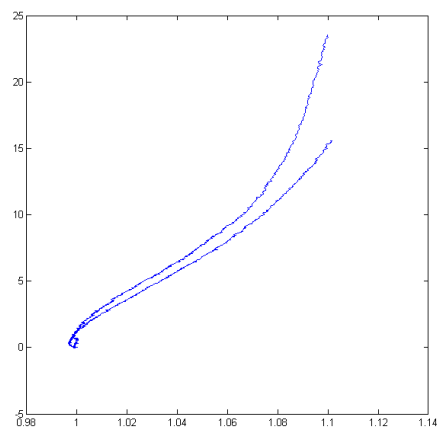
(a) Plot of all 10% cycles.



(b) Separate graphs for all cycles.

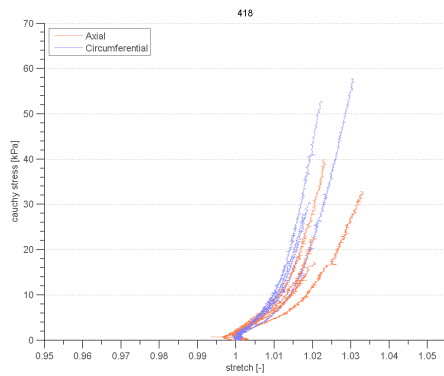


(c) Preconditioning cycles.

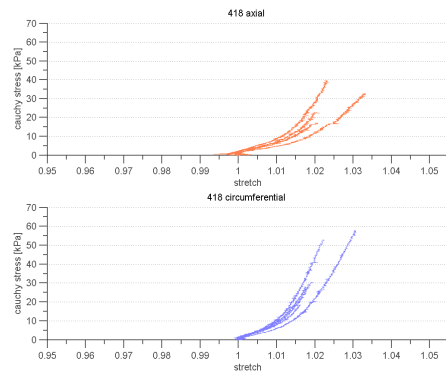


(d) Measuring cycle.

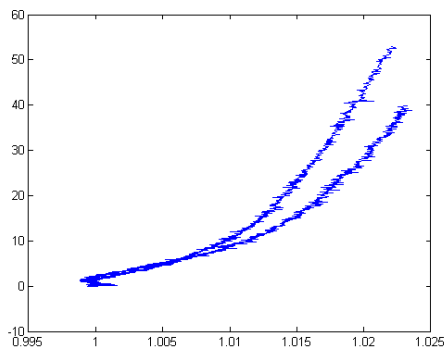
Figure 44: Biaxial testing plots for 417-3 sample.



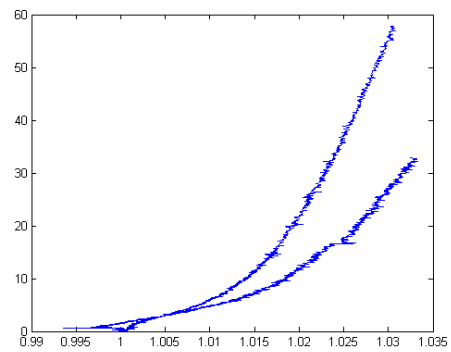
(a) Plot of all 5% cycles.



(b) Seperate graphs for all cycles.

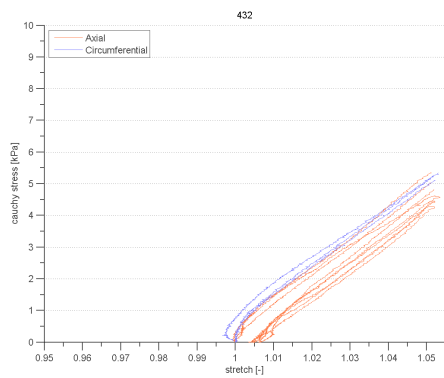


(c) Preconditioning.

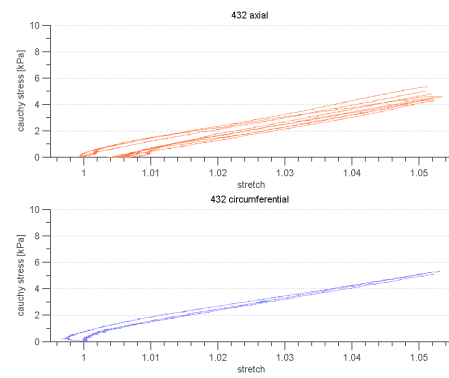


(d) Measuring cycle.

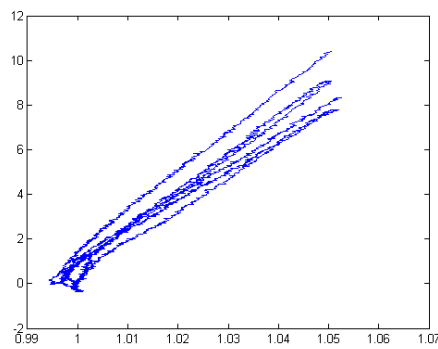
Figure 45: Biaxial testing plots for 418-2 sample.



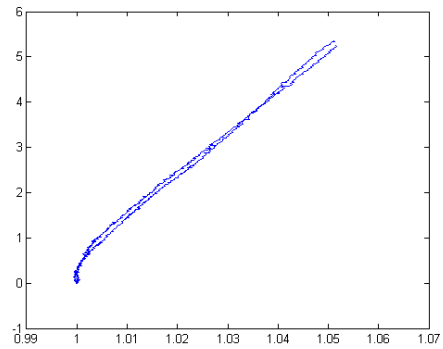
(a) Plot of all 5% cycles.



(b) Separate graphs for all cycles.

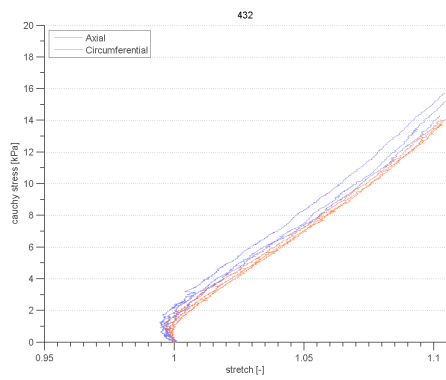


(c) Preconditioning.

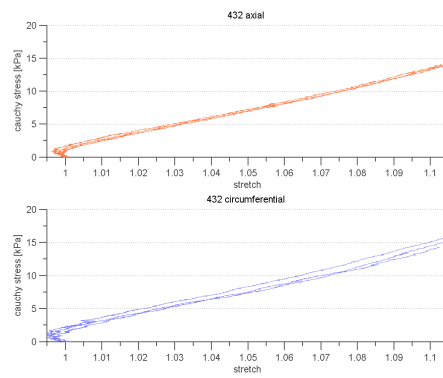


(d) Measuring cycle.

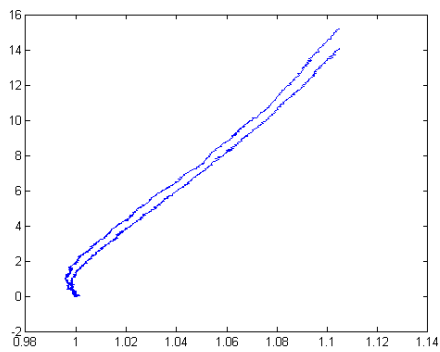
Figure 46: Biaxial testing plots for 432-2 sample.



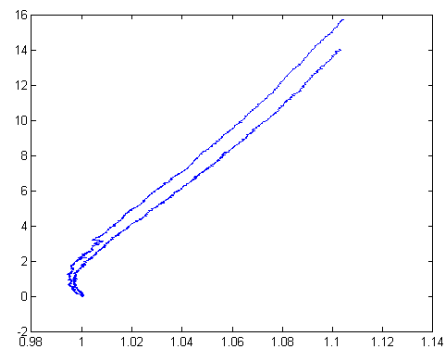
(a) Plot of all 10% cycles.



(b) Separate graphs for all cycles.

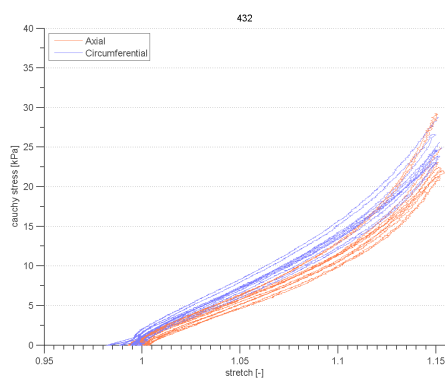


(c) Preconditioning cycles.

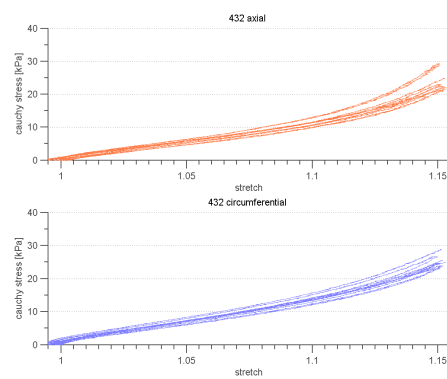


(d) Measuring cycle.

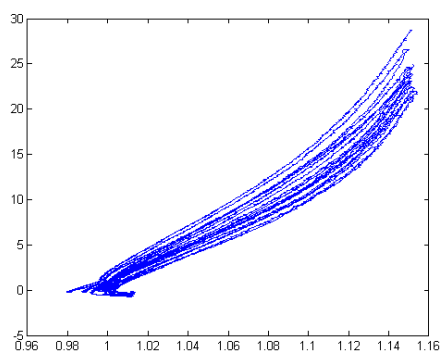
Figure 47: Biaxial testing plots for 432-3 sample.



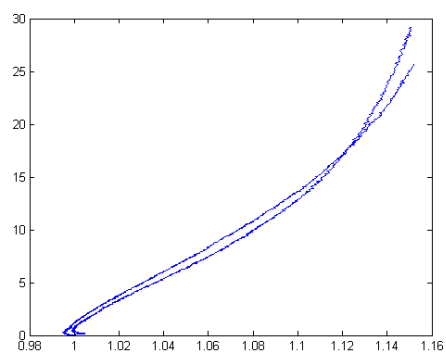
(a) Plot of all 15% cycles.



(b) Separate graphs for all cycles.



(c) Preconditioning cycles.



(d) Measuring cycle.

Figure 48: Biaxial testing plots for 432-4 sample.

Abbreviations

CB	Cuprolinic Blue
CCD	Charge-coupled Device
ECM	Extracellular Matrix
EDX	Energy-dispersive X-ray
ELE	Elastica Lamina Externa
GA	Glutaraldehyde
GAG	Glycosaminoglycan
IEL	Internal Elastica Lamina
LDL	Low-density Lipoprotein
PBS	Phosphate-buffered Saline
PG	Proteoglycan
ROI	Region of Interest
SHG	Second-harmonic Generation
SHIM	Second-harmonic Imaging Microscopy
SLRP	Small Leucine Rich Proteoglycans
SMC	Smooth Muscle Cell
TEM	Transmission Electron Microscope
UA	Uranyl Acetate

References

- [1] J. M. Clark and S. Glagov. Transmural organization of the arterial media. The lamellar unit revisited. *Arteriosclerosis, Thrombosis, and Vascular Biology*, 5(1):19–34, 1985.
- [2] R. F. Egerton. *Physical Principles of Electron Microscopy*. Springer Science+Business Media, Inc., 2005.
- [3] A. Eilaghi, J. G. Flanagan, G. W. Brodland, and C. R. Ethier. Strain Uniformity in Biaxial Specimens is Highly Sensitive to Attachment Details. *Journal of Biomechanical Engineering*, 131(9), 2009.
- [4] M. S. Fernández-Alfonso, B. Somoza, D. Tsvetkov, A. Kuczmanski, M. Dashwood, and M. Gil-Ortega. Role of Perivascular Adipose Tissue in Health and Disease. In *Comprehensive Physiology*, pages 23–59. John Wiley & Sons, Inc., Hoboken, NJ, USA, 2017.
- [5] P. Fratzl, editor. *Collagen Structure and Mechanics*. Springer US, Boston, MA, 2008.
- [6] G. A. Holzapfel. *Mechanics of Biological Tissues*. Lecture notes, Graz University of Technology, 2014.
- [7] G. A. Holzapfel, T. C. Gasser, and R. W. Ogden. A new constitutive framework for arterial wall mechanics and a comparative study of material models. In *Journal of Elasticity. The Physical and Mathematical Science of Solids*, 2001.
- [8] G.A. Holzapfel. Collagen in Arterial Walls: Biomechanical Aspects. In M. K. Franklin, L. C. K. Hui, and D. S. Wong, editors, *Collagen. Structure and Mechanics*, pages 285–324. Springer, New York, NY, 1 edition, 2008.
- [9] J. D. Humphrey. *Cardiovascular Solid Mechanics: Cells, Tissues, and Organs*. page 757, 2002.
- [10] J. D. Humphrey, R. K. Strumpf, and F. C. Yin. Biaxial mechanical behavior of excised ventricular epicardium. *American Journal of Physiology-Heart and Circulatory Physiology*, 259(1), jul 1990.

- [11] C. M. Kelleher, S. E. McLean, and R. P. Mecham. Vascular Extracellular Matrix and Aortic Development. *Current Topics in Developmental Biology*, 62:153–188, 2004.
- [12] R. R. Kolvenbach, R. Karmeli, L. S. Pinter, Y. Zhu, F. Lin, S. Wassiljew, and M. Meyer-Gaessner. Endovascular management of ascending aortic pathology. *Journal of Vascular Surgery*, 53(5):1431–1437, 2011.
- [13] R. H. Lange and J. Bloedorn. *Das Elektronenmikroskop TEM + REM*. George Thiem Verlag KG, 1 edition, 1981.
- [14] P. Libby, P. M. Ridker, and G. K. Hansson. Progress and challenges in translating the biology of atherosclerosis. *Nature*, 473(7347):317–325, 2011.
- [15] A. J. Lusis. Atherosclerosis. *Nature*, 407(6801):233–41, 2000.
- [16] K. A. McCullagh and G. Balian. Collagen characterisation and cell transformation in human atherosclerosis. *Nature*, 258(5530):73–75, 1975.
- [17] R. McIntosh, D. Nicastro, and D. Mastronarde. New views of cells in 3D: an introduction to electron tomography. *Trends in Cell Biology*, 15(1):43–51, jan 2005.
- [18] D. Serwas and A. Dammermann. Ultrastructural analysis of *Caenorhabditis elegans* cilia. In *Methods in Cell Biology*, volume 129, pages 341–367. Elsevier, 2015.
- [19] G. Sommer. *Mechanical Properties of Healthy and Diseased Human Arteries and Related Material Modeling*. PhD thesis, Graz University of Technology, 2008.
- [20] I. Tabas. Macrophage death and defective inflammation resolution in atherosclerosis. 10(1):36–46, 2010.
- [21] I. Tabas, K. J. Williams, and J. Boren. Subendothelial Lipoprotein Retention as the Initiating Process in Atherosclerosis: Update and Therapeutic Implications. *Circulation*, 116(16):1832–1844, 2007.
- [22] A. D. Theocharis and N. K. Karamanos. Decreased biglycan expression and differential decorin localization in human abdominal aortic aneurysms. *Atherosclerosis*, 165(2):221–230, 2002.

-
- [23] M. J. Thubrikar. *Vascular Mechanics and Pathology*. Springer US, Boston, MA, 2007.
- [24] S. Vesentini, A. Redaelli, and F. M. Montevvecchi. Estimation of the binding force of the collagen molecule-decorin core protein complex in collagen fibril. *Journal of Biomechanics*, 38(3):433–443, 2005.
- [25] K. Von Der Mark. Localization of Collagen Types in Tissues*. *Int. Rev. Connect. Tissue. Res.*, 9:265–324, 1981.
- [26] T. N. Wight and M.J. Merrilees. Proteoglycans in Atherosclerosis and Restenosis: Key Roles for Versican. *Circulation Research*, 94(9):1158–1167, 2004.
- [27] C. Williams, J. Liao, E. M. Joyce, B. Wang, J. B. Leach, M. S. Sacks, and J. Y. Wong. Altered structural and mechanical properties in decellularized rabbit carotid arteries. *Acta Biomaterialia*, 5(4):993–1005, 2009.
- [28] H. Wolinsky and S. Glagov. Nature of species differences in the medial distribution of aortic vasa vasorum in mammals. *Circulation research*, 1967.
- [29] L. Y. Yao, C. Moody, E. Schönherr, T. N. Wight, and L. J. Sandell. Identification of the proteoglycan versican in aorta and smooth muscle cells by DNA sequence analysis, in situ hybridization and immunohistochemistry. *Matrix Biology*, 14(3):213–225, 1994.